

Delayed-mode quality control of oxygen, nitrate and pH data on SOCCOM biogeochemical profiling floats

Tanya Lea Maurer¹, Josh N. Plant¹, and Kenneth S. Johnson²

¹MBARI

²Monterey Bay Aquarium Res. Inst.

November 22, 2022

Abstract

The Southern Ocean Carbon and Climate Observations and Modeling (SOCCOM) project has deployed 194 profiling floats equipped with biogeochemical (BGC) sensors, making it one of the largest contributors to global BGC-Argo. Post-deployment quality control of float-based oxygen, nitrate, and pH data is a crucial step in the processing and dissemination of such data, as in-situ chemical sensors remain in early stages of development. In-situ calibration of chemical sensors on profiling floats using atmospheric reanalysis and empirical algorithms have been shown to bring accuracy to within 3 $\mu\text{mol O}_2 \text{ kg}^{-1}$, 0.007 pH units, and 0.5 $\mu\text{mol NO}_3^- \text{ kg}^{-1}$. Routine quality control efforts utilizing these methods can be conducted manually through visual inspection of data to assess sensor drifts and offsets, but more automated processes are preferred to support the growing number of BGC floats and reduce subjectivity among delayed-mode operators. Here we present a methodology and accompanying software designed to easily visualize float data against select reference datasets and assess quality control adjustments within a quantitative framework. The software is intended for global use and has been used successfully in the post-deployment calibration and quality control of over 250 BGC floats, including all within the SOCCOM array. Results from validation of the proposed methodology are also presented which can provide a metric for tracking data adjustment quality through time.

1 **Delayed-mode quality control of oxygen, nitrate and pH data on SOCCOM**
2 **biogeochemical profiling floats**

3 **Tanya L. Maurer¹, Joshua N. Plant², and Kenneth S. Johnson³**

4 ^{1,2,3} Monterey Bay Aquarium Research Institute, 7700 Sandholdt Road, Moss Landing, CA
5 95039.

6 **Key Points:**

- 7 • A methodology and related software for visualizing biogeochemical data against
8 references aids in correcting data for shifts in calibration
9 • Described methods bring data accuracies to within the range required for climate studies
10 and remain applicable over the lifetime of a float
11 • A standardized approach to quality control supports cross-platform data management and
12 routine monitoring of fleet-wide sensor performance

13 **Abstract**

14 The Southern Ocean Carbon and Climate Observations and Modeling (SOCCOM) project has
15 deployed 194 profiling floats equipped with biogeochemical (BGC) sensors, making it one of the
16 largest contributors to global BGC-Argo. Post-deployment quality control of float-based
17 oxygen, nitrate, and pH data is a crucial step in the processing and dissemination of such data, as
18 in-situ chemical sensors remain in early stages of development. In-situ calibration of chemical
19 sensors on profiling floats using atmospheric reanalysis and empirical algorithms have been
20 shown to bring accuracy to within $3 \mu\text{mol O}_2 \text{ kg}^{-1}$, 0.007 pH units, and $0.5 \mu\text{mol NO}_3^- \text{ kg}^{-1}$.
21 Routine quality control efforts utilizing these methods can be conducted manually through visual
22 inspection of data to assess sensor drifts and offsets, but more automated processes are preferred
23 to support the growing number of BGC floats and reduce subjectivity among delayed-mode
24 operators. Here we present a methodology and accompanying software designed to easily
25 visualize float data against select reference datasets and assess quality control adjustments within
26 a quantitative framework. The software is intended for global use and has been used
27 successfully in the post-deployment calibration and quality control of over 250 BGC floats,
28 including all within the SOCCOM array. Results from validation of the proposed methodology
29 are also presented which can provide a metric for tracking data adjustment quality through time.
30

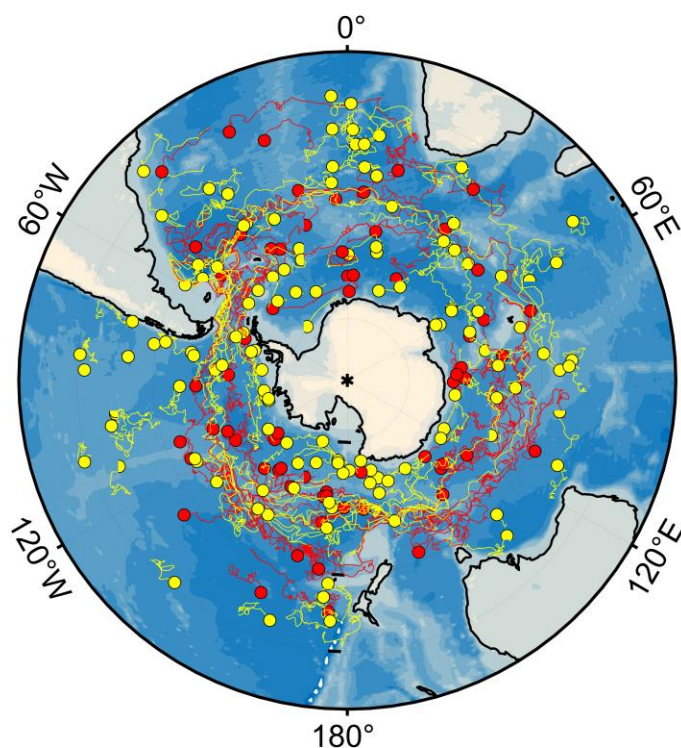
31 **Plain Language Summary**

32 The amount of chemical oceanographic data available to researchers is rapidly increasing thanks
33 to robotic drifting floats such as those deployed through the Southern Ocean Carbon and Climate
34 Observations and Modeling (SOCCOM) project. Because these floats live the entirety of their
35 life at sea, ensuring that the sensors are working as expected and that the quality of the data
36 returned is fit for scientific use must be done remotely. This paper describes the approaches and
37 accompanying software used to assess performance of oxygen, nitrate and pH sensors on
38 profiling floats and correct for any shifts in sensor performance through the life of the float. An
39 independent validation of the proposed methods is also presented which provides an added level
40 of confidence to the described methods and overall quality of the dataset.

41 **1 Introduction**

42 The Southern Ocean Carbon and Climate Observations and Modeling (SOCCOM) project has
43 finished its sixth year reaching a total of 194 biogeochemical (BGC)-Argo profiling floats
44 deployed throughout the Southern Ocean (Fig. 1). Funded by the US National Science
45 Foundation (NSF) Office of Polar Programs, this novel basin-scale network of biogeochemical
46 sensors has filled one of the largest observational gaps in the global ocean. Due to the success of
47 the current program, the SOCCOM project has been renewed for an additional four years, with
48 the goal of deploying 120 more BGC profiling floats south of 30S. In addition, the NSF has
49 funded the Global Ocean Biogeochemistry (GO-BGC) Array, which will extend the current
50 BGC-Argo program considerably through the deployment of an additional 500 floats throughout
51 the global ocean. Emerging data from floats within the SOCCOM array have already expanded
52 our understanding of the Southern Ocean's role in the global carbon cycle and have improved the
53 capability of ocean models to predict future change (Bushinsky et al., 2019a; Gray et al., 2018;
54 Russell et al., 2018; Swart et al., 2019; Verdy & Mazloff, 2017; Williams et al., 2018). Key to
55 these advancements has been the underlying quality of the supporting dataset which relies on

56 pre-deployment sensor calibration and post-deployment quality control (QC), bringing sensor
 57 accuracies to within the narrow range required for climate studies (Johnson et al., 2017).
 58



59 **Figure 1.** Current location (circles) and associated trajectories (lines) from floats within the
 60 SOCCOM array, as of December, 2020. Both operational (yellow) and inactive (red) floats are
 61 shown. Historical data from inactive floats remains a valuable part of the SOCCOM dataset.
 62
 63

64 Operational procedures for post-deployment processing of CTD data from the Argo array are
 65 well established. A number of real-time checks constitute the first level of quality control, many
 66 of which have been adopted for BGC data as well (Schmechtig et al., 2016). Salinity profiles
 67 from Argo floats are also subject to various delayed-mode assessments that typically apply
 68 interpolation methods to relate float data to a climatology (Gaillard et al., 2009; Guinehut et al.,
 69 2009; Owens & Wong, 2009; Wong et al., 2003). Argo salinity data have been estimated to be
 70 accurate to 0.01 PSU, after delayed-mode adjustments, and temperature and pressure data are
 71 generally thought of as acceptable for use in data assimilation and other direct applications prior
 72 to receiving any delayed-mode assessment (Wong et al., 2020).

73 In contrast, in situ chemical sensors for measuring oxygen, nitrate and pH on BGC-Argo
 74 floats represent newer technologies that require significantly more quality control. Generally,
 75 the scientific use of raw, unadjusted BGC-Argo float data is not recommended. The real-time
 76 and delayed-mode adjustment processes greatly improve the quality of the BGC sensor data and
 77 result in a data set that is suited for research in a variety of applications. Various delayed-mode
 78 methods for BGC sensor recalibration and quality control for oxygen, pH and nitrate have been
 79 suggested (Bittig et al., 2018a; Johnson et al. 2013; 2015; 2017; Takeshita et al., 2013; Williams
 80 et al., 2016) but integrating the suite of methodologies into a coherent framework that can be
 81 used operationally across a fleet has proven challenging. Producing science-quality

82 biogeochemical data requires consistent and traceable correction methods that can be adopted
83 globally across all data centers.

84 In this paper we present the methodology developed as part of the SOCCOM program to
85 assess oxygen, nitrate, and pH sensor gain, drifts and offsets in delayed-mode. The two
86 accompanying MATLAB tools, SAGE (SOCCOM Assessment and Graphical Evaluation) and
87 SAGE-O₂, are also described. The magnitude of required adjustments within the SOCCOM
88 array and an independent validation of described methods are also discussed.

89 2 SOCCOM float array

90 The SOCCOM array of profiling floats includes both Teledyne/Webb Research (TWR)
91 APEX and Sea-Bird Scientific (SBE) Navis floats. All SOCCOM floats utilize Iridium two-way
92 satellite communication and are outfitted with ice-avoidance software developed at the
93 University of Washington (UW) (Riser et al., 2018; Wong & Riser, 2011). For profiles taken
94 while under ice, geographic coordinates cannot be obtained so latitude and longitude are
95 estimated through linear interpolation. All SOCCOM floats are programmed to perform the
96 nominal Argo mission of 10-day profile frequency from a maximum depth of 2000m with an
97 interim park depth of 1000m.

98 The SOCCOM floats carry a suite of biogeochemical sensors, with sensor models
99 varying slightly between the two platforms (Table 1). The ISUS nitrate (Johnson & Coletti,
100 2003) and Deep-Sea DuraFET pH (Johnson et al., 2016) sensors used on APEX floats are
101 primarily built and calibrated at the Monterey Bay Aquarium Research Institute (MBARI). pH
102 sensors from SBE are also deployed on APEX floats. These receive pressure and temperature
103 calibrations at SBE, and a final pH calibration at MBARI. All other sensors listed in Table 1
104 receive factory-calibration direct from the manufacturer. Both sensor categories (MBARI-
105 calibrated or manufacturer-calibrated) can suffer from shifts in laboratory calibration leading to
106 changes in performance that manifest as sensor offsets or drifts in the field.
107
108

Parameter	Navis sensor model	APEX sensor model
T, S, P	SBE 41N	SBE 41CP
Oxygen	SBE 63 Optode	Aanderaa Optode (3830 or 4330)
Nitrate	² SUNA	¹ ISUS
pH	Deep-Sea DuraFET from Sea-Bird	Deep-Sea DuraFET
Bio-optics	WET Labs MCOMS (chl-a fluorometer, 700nm backscatter, FDOM)	WET Labs ECO-FLBB AP2 (chl-a fluorometer, 700nm backscatter)

109 ¹In-Situ Ultraviolet Spectrophotometer

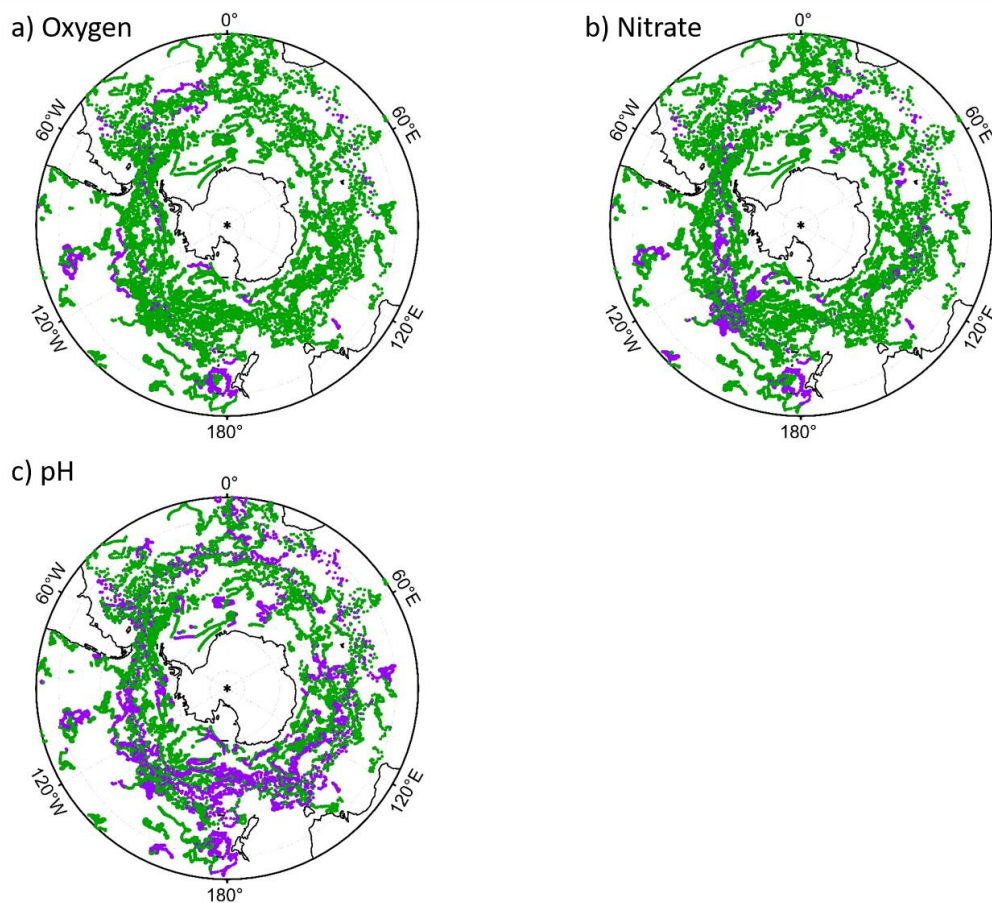
110 ²Submersible Ultraviolet Nitrate Analyzers

111 **Table 1.** Sensor models used on Sea-Bird Navis and MBARI/UW-built Teledyne-Webb APEX
112 floats in SOCCOM.

113

114 Automatic QC procedures are applied in real-time to flag grossly erroneous data within
115 the SOCCOM array. These tests roughly follow the Argo real-time tests for BGC data as
116 outlined in Schmechtig et al. (2016). Fig. 2 shows SOCCOM float tracks colored by data

117 quality. Points along a float track marked in purple represent profiles where >50% of the data
 118 has been marked “bad” by one of the automated QC tests. Of the three parameters shown, pH
 119 sensor data have the highest number of “bad” quality flags, at 35.59% of the data.
 120



121
 122 **Figure 2.** SOCCOM float tracks colored by data quality for (a) oxygen, (b) nitrate, and (c) pH.
 123 Points along a float track marked in purple (green) represent profiles where >50% of the data has
 124 been marked “bad” (“good”) by one of the automated QC tests.
 125

126 After passing the real-time quality checks, oxygen, nitrate and pH data that are
 127 considered adjustable can be brought up to the accuracy level required for global biogeochemical
 128 studies through relatively simple correction procedures (Johnson et al., 2018b; Thierry et al.,
 129 2018b). This represents the second level of quality control (Bittig et al., 2019). In the next
 130 sections, the delayed-mode procedures and accompanying software tools used in the adjustment
 131 of oxygen, nitrate and pH data on a SOCCOM float are presented.

132 **3 Adjustment of oxygen data**

133 3.1 Gain adjustments for optodes

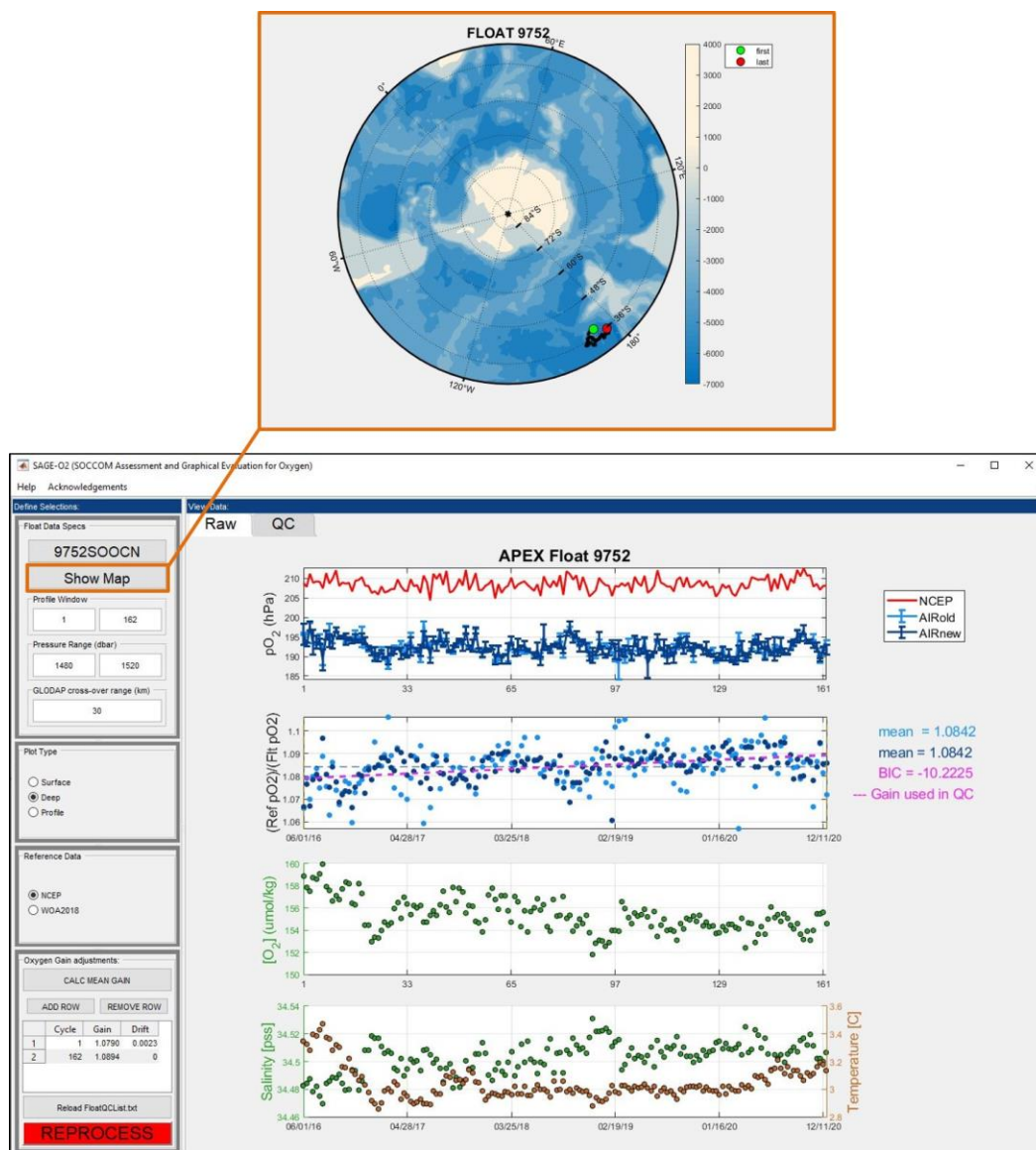
134 The delayed-mode correction procedure for biogeochemical data on a SOCCOM float
 135 begins with oxygen. This is because the deep reference fields used in nitrate and pH quality
 136 control (described in Section 4) are generated from empirical algorithms that require accurate

137 oxygen measurements (along with other core variables and position information) as input
138 parameters. Takeshita et al. (2013) have shown that the raw oxygen data from floats can be in
139 error by as much as 20% of surface water oxygen saturation due to storage drift. Following
140 Johnson et al. (2015), oxygen concentrations can be corrected using a multiplicative gain factor,
141 G , to reduce the effects of storage drift and improve the accuracy of the sensor (for additional
142 information on optode storage drift see Bittig et al. (2018a) and D'Asaro & McNeil (2013)):
143

$$144 \quad [O_2]_{corr} = G \times [O_2]_{raw} \quad (2)$$

145
146 There is some evidence in the literature that a slope correction on oxygen concentration could
147 potentially be improved by the inclusion of an intercept, especially in regions of near-zero
148 oxygen levels (Bittig & Kortzinger, 2015; Bushinsky et al., 2016; Drucker & Riser, 2016;
149 Nicholson & Feen, 2017). However, such corrections appear to be small ($<1 \mu\text{mol kg}^{-1}$), based
150 on an assessment of 20 floats in the Arabian Sea and Bay of Bengal (Johnson et al., 2019) and
151 are thus not implemented within the SOCCOM program.

152 SAGE-O₂ is the MATLAB Graphical User Interface (GUI) developed at MBARI to assist
153 in deriving oxygen optode gain corrections by comparing oxygen data from a float to various
154 reference datasets, including measurements of oxygen partial pressure in the atmosphere. An
155 image of the interface, including the plot display window and user-controlled sidebar is shown in
156 Fig. 3 for SOCCOM float 9752 (WMO 5904694) in the Southwest Pacific, east of New Zealand.
157 The top panel of the interface displays a time series of float data (blue) in comparison to the user-
158 selected reference (red). Details related to the calculation of the gain factor, G , over the lifetime
159 of a float, as implemented through the software, are described further below.
160
161



162
163
164
165
166

Figure 3. SAGE-O₂ software interface showing results of the calibration for sample float 9752, WMO 5904694. The map display functionality is also indicated.

167

3.1.1 Gain computation using in-air oxygen with NCEP/NCAR Reanalysis

168 In-air calibration of oxygen optodes onboard profiling floats has been shown to bring
169 accuracy to within 1% and is currently the operational standard (Johnson et al., 2015). For floats
170 with in-air measurement capabilities, an estimate of atmospheric pressure must be available to
171 compute the local oxygen partial pressure. The product referenced for oxygen gain computation
172 within the SAGE-O₂ software is NCEP/NCAR Reanalysis-1 six-hourly surface pressure (Kalnay
173 et al., 1996). This is a Gaussian gridded product with units of Pascals, which are converted to
174 hectopascals (millibar equivalent) prior to proceeding. The NCEP atmospheric surface pressure
175 (P_{NCEP}) values are interpolated to the time and location of the float's surfacing. Values are then
176 converted to oxygen partial pressure based on the assumption that the atmosphere is 100%

177 saturated with water vapor at the sea surface (equation (3)). The water vapor pressure (p_{H_2O} , in
 178 hPa) is calculated using equation (4), where T represents temperature in degrees Celsius
 179 (Aanderaa Instruments, 2017).

$$181 \quad p_{O_2} = (P_{NCEP} - p_{H_2O}) \times 0.20946 \quad (3)$$

$$182 \quad p_{H_2O} = e^{\left[52.57 - \left(\frac{6690.9}{T+273.15}\right) - 4.681 \times \ln(T+273.15)\right]} \quad (4)$$

185
 186 The sensor gain that is estimated from air oxygen for each individual profile, i , is then computed
 187 using equation (5), as outlined in Johnson et al. (2015):

$$188 \quad G_i = p_{O_2NCEP} / p_{O_2FLOAT} \quad (5)$$

190
 191 where p_{O_2NCEP} follows from equation (2) and p_{O_2FLOAT} is the partial pressure of oxygen
 192 computed from the float (reported in millibars). The overall gain factor, G, used to correct all in
 193 water oxygen observations is then the mean of the n individual G_i values.

194 Mean gain values over the float's life are displayed within the SAGE-O₂ interface in blue
 195 to the right of the plot panels (Fig. 3). Note that at the start of the SOCCOM program, APEX
 196 floats were programmed to take a single in-air oxygen reading with each surfacing that was
 197 associated with the telemetry phase of the cycle. A subsequent upgrade to the mission
 198 programming was initialized such that the optodes on APEX floats take a sequence of in-air
 199 measurements at each surfacing at the end of ascent (4 subsurface measurements followed by 8
 200 measurements in air after inflation of the air-bladder). Therefore, the majority of APEX floats in
 201 the SOCCOM program have 2 sets of in-air measurements: one associated with the telemetry
 202 phase (light blue in the GUI interface), and another larger set associated with the in-air
 203 measurement series (dark blue in the interface). Both of these are plotted in the GUI for
 204 comparison. Average gain between the two sets differs by less than 0.1 % fleet-wide.

205 In the future the SAGE-O₂ software may be upgraded to utilize the now real-time
 206 NCEP/DOE-R2 reanalysis product. Additional reanalysis products from other centers are also
 207 available, including the European Centre for Medium-Range Weather Forecasts (ECMWF)
 208 ERA5 reanalysis. The ERA5 product utilizes a more state-of-the-art (4D-variational) data
 209 assimilation system but its data latency (3 month lag for quality assured updates) may limit
 210 timely delayed-mode QC operations. The absolute uncertainty in reanalysis surface pressure
 211 fields from different products can be difficult to fully quantify although a comparison of NCEP
 212 and ECMWF operational models by Salstein et al. (2008) found that rms differences between
 213 surface pressure and shipboard observational stations were between 2 and 5 hPa in Southern
 214 latitudes with minimal difference between the two products, especially in more recent years.
 215 Surface pressure uncertainties of this magnitude roughly translate to less than 0.5% change in
 216 corrected O₂ measurements on individual floats.

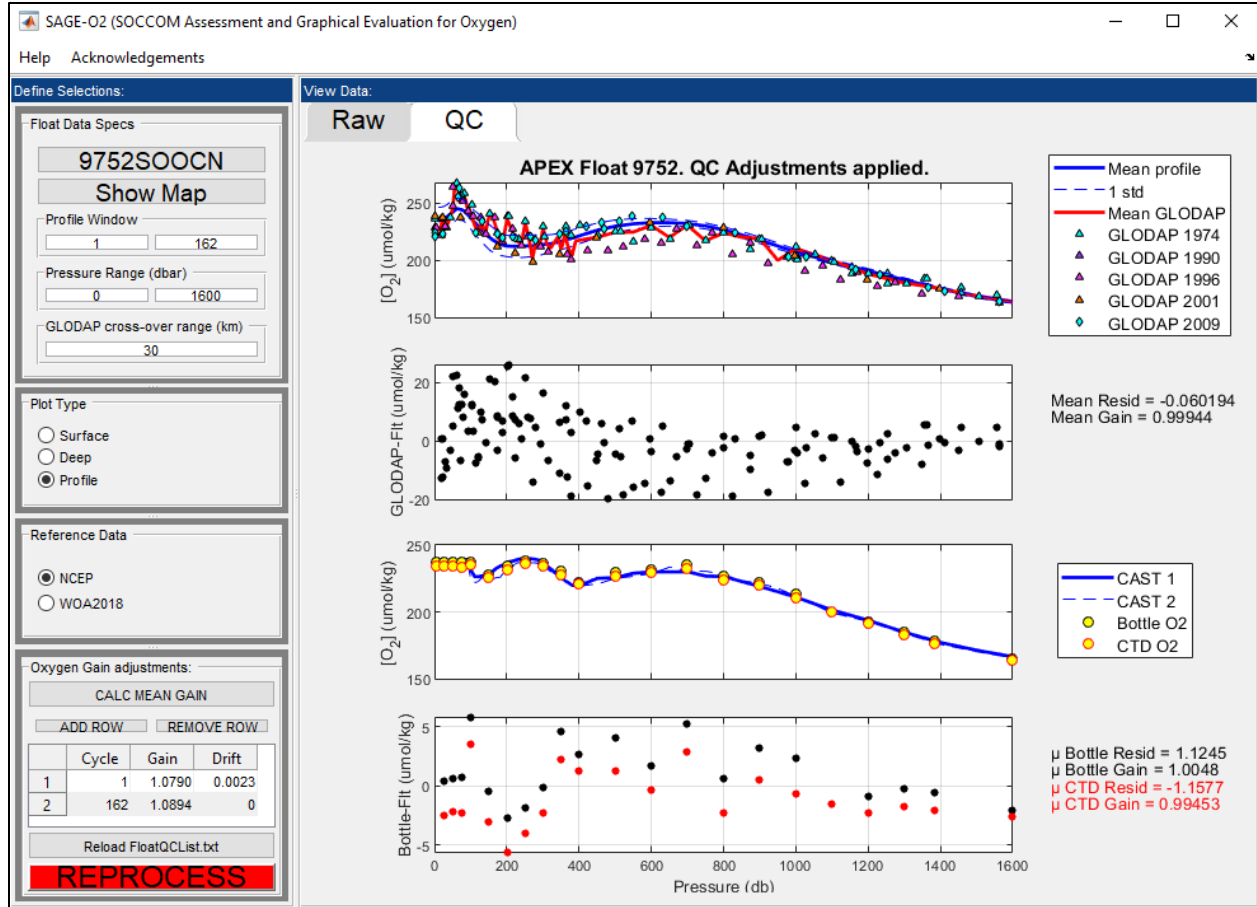
217 3.1.2 Gain computation using shipboard bottle data

218 The SBE63 optodes onboard SOCCOM Navis floats are plumbed in line with the
 219 pumped CTD flow stream and are thus not fully exposed to ambient air during surfacing. In-situ
 220 calibration of these floats thus relies on comparison to high-quality Winkler titrations from

221 shipboard samples taken at the time of float deployment. The Winkler oxygen are generated
222 primarily on GO-SHIP cruises or by research groups that regularly participate in GO-SHIP
223 cruises and they are considered to be of a quality consistent with GO-SHIP measurements (Hood
224 et al., 2010 state a target accuracy of 2σ less than 0.5% of the largest oxygen concentration found
225 in the ocean). Comparisons of the float and bottle data can be viewed through the software (Fig.
226 4). We focus on the upper 50m near the surface where oxygen is close to 100% saturated and the
227 vertical gradients are small. A comparison of average gain values derived using shipboard
228 Winkler measurements versus in-air samples for 97 SOCCOM APEX floats shows a mean
229 difference (float minus bottle) of -0.31% (standard deviation of 2.2%). This suggests that there is
230 no large systematic bias for Navis floats when optodes are calibrated using bottle data.

231 In addition to providing an alternative approach to in-situ optode calibration, comparison
232 to shipboard data offers a simple and independent means for validating gain values derived from
233 other methods. The gain correction for the float shown in Fig. 3 was performed using in-air
234 measurement data as described in Section 3.1.1. Fig. 4 shows data from this float in profile
235 view. Pressure is along the x-axis for all plot panels. The top two panels show mean float data
236 (solid blue line) along with GLODAPv2 profile data that are within a 30km radius, and the
237 computed residuals. The bottom two panels show the float's first and second profiles (blue)
238 along with shipboard Winkler and CTD oxygen data (circles), and computed residuals. Note that
239 the 'QC' tab is selected, thus all float data in the display have been adjusted using the computed
240 gain shown in Fig. 3. If the 'Raw' tab was chosen, the float profile would have no adjustments
241 applied. The small positive bias shown in reference to the bottle data is due to temporal
242 mismatch between the shipboard data and float measurements within high-gradient regions of the
243 profile. The mean residual (bottle-float) is $1.245 \mu\text{mol kg}^{-1}$. The mean residual against all
244 GLODAPv2 data within 30 km is $-0.060 \mu\text{mol kg}^{-1}$, although the range is larger than the
245 hydrocast data due to the larger time range included in the matchup criteria.

246



247

248 **Figure 4.** A comparison of adjusted oxygen data to GLODAPv2 (top two panels) and shipboard
 249 hydrocast matchups (lower two panels), as viewed through the SAGE-O₂ interface for
 250 UW/MBARI float 9752 (WMO 5904694).

251 3.1.3 Gain computation using World Ocean Atlas climatology (WOA)

252 For floats incapable of taking in-air oxygen measurements, and when shipboard reference
 253 data are not yet available, a preliminary optode gain correction factor can be derived within the
 254 SAGE-O₂ GUI using WOA percent oxygen saturation in surface water. This method follows
 255 Takeshita et al. (2013), which suggest an accuracy of 1-3% for sensors calibrated against WOA
 256 values. Percent saturation from the float is calculated following equation (7) below, where the
 257 solubility of oxygen (O_{2Sol}) is computed as a function of temperature and salinity following
 258 Garcia & Gordon (1992) equation 8 (omitting erroneous term $[A3 * T_s^2]$) and using solubility
 259 constants from Benson and Krause (1984) (see equation 8 and Table 1 in Garcia & Gordon,
 260 1992). Individual gain values, G_i , are then computed using equation (8), where $\%Sat_{WOA}$ and
 261 $\%Sat_{Float}$ represent the mean WOA and mean float percent saturation values for the upper 25m
 262 of the profile, respectively.

263

264

$$\%Sat = [O_2]/[O_{2Sol}] \times 100 \quad (7)$$

265

266

$$G_i = \%Sat_{WOA}/\%Sat_{Float} \quad (8)$$

267
 268 The overall gain factor, G , is calculated as the mean of the individual gain values (G_i)
 269 computed for each cycle. A comparison of gain factors computed using WOA percent saturation
 270 versus NCEP reanalysis air pressure as reference for 95 floats with in-air measurement
 271 capabilities shows a bias between the methods of 1.4% with a standard deviation near 2%. The
 272 largest differences occur in floats near seasonal sea ice or very close to the coast where WOA
 273 reference climatology data is limited and/or seasonally biased. Note that for many floats within
 274 the global BGC Argo array, this method is the most accessible option for data managers and
 275 should be applied wherever possible as a first-order correction.

276 3.2 Drift in optode gain

277 The effects of pre-deployment storage drift are readily apparent across the majority of
 278 optodes used on profiling floats. Oxygen data from all Aanderaa and Sea-Bird optodes onboard
 279 SOCCOM floats require gain correction, with a fleet-wide mean gain correction of 7.0 ± 4.6 (1σ)
 280 %. While an optode's stability once deployed is substantially smaller, it is less predictable
 281 (Bittig & Kortzinger, 2015; Bittig & Kortzinger, 2017; Bushinsky et al., 2016; Johnson et al.,
 282 2015). Bittig et al. (2018a) provides a thorough review on this topic, and suggests that individual
 283 optodes may exhibit significant post-deployment drift of up to $\pm 0.6\%/yr$. If not accounted for,
 284 such drift could lead to significant biases in certain biogeochemical analyses such as air-sea
 285 fluxes.

286 Characterizing the amount of optode drift is possible within the SAGE-O₂ software
 287 through comparison against reference values over time. This method was recently put into
 288 practice for select floats within the SOCCOM fleet. The software allows the user to auto-
 289 calculate the drift relative to a reference such as NCEP. The computed offset (initial gain), b ,
 290 and slope (drift), m , are calculated using a model I regression of computed gain on each cycle
 291 against cycle time. The gain value applied at each cycle (following equation 1) then becomes:

$$292 \quad G_{i=1:k} = b + m(\Delta T) \quad (9)$$

293 where ΔT is the time, in years, elapsed since the first cycle (or time at which the drift began). If
 294 the chosen ending node at cycle k is not the final cycle reported from the float upon assessment,
 295 a drift assessment on the subsequent segment (cycles $i=k:n$) is automatically performed. The
 296 slope of the second segment, m_2 , is found by first subtracting the recomputed gain at the end of
 297 the first segment (G_k) from individual gains, g_i , of segment 2, and then regressing segment 2
 298 through the origin. This can be expressed as

$$299 \quad m_2 = \frac{\sum_{i=k}^n (g_i - G_k) * x_i}{\sum_{i=k}^n x_i^2} \quad (10)$$

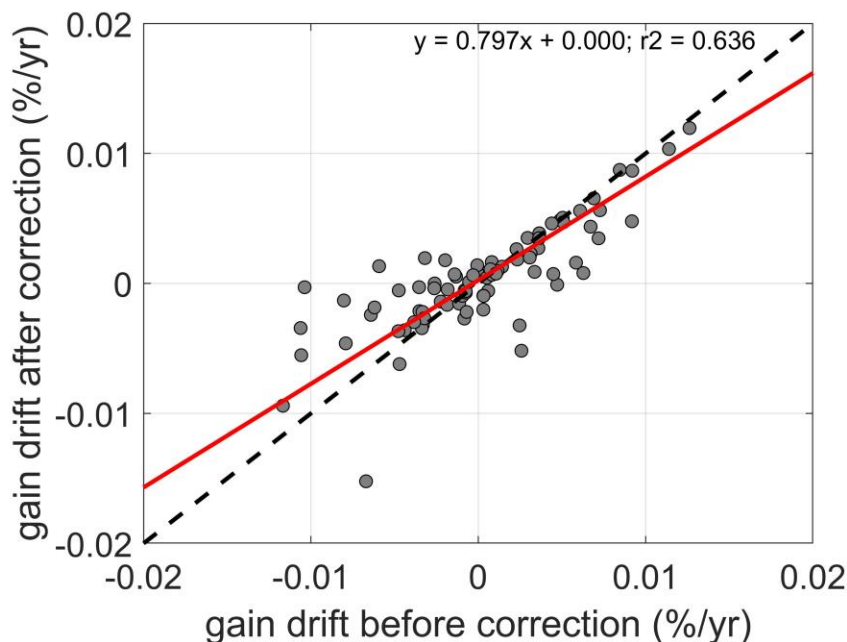
300 where x represents the time elapsed since the ending cycle of segment 2. This method results in
 301 drifting gains that remain continuous throughout segments. However, note that drift assessment
 302 within the GUI (and especially multi-segment drifts) should be limited to advanced users. It is
 303 recommended that drift assessment be performed only after a sufficient amount of data has been
 304 received (optimally at least 2 years). Care must be taken in order to prevent correcting for an
 305 apparent drift that has been influenced by a seasonal cycle.

310 Within the GUI there are two methods to test whether or not a computed drift over the
 311 lifetime of a float is statistically robust. Upon auto-computation of the drift, a two-tailed T-test is
 312 performed to assess whether the calculated slope is significantly different than zero at the 95%
 313 confidence interval (results are returned on screen). Additionally, on the right-side panel in the
 314 interface, the GUI reports the computed Bayesian Information Criteria (BIC) (Schwarz, 1978)
 315 following Equation 11 below, where SSR represents the sum of squared residuals of the model, K
 316 is the number of model parameters, and n represents the number of data points. The BIC weighs
 317 the number of predictors within a model against the goodness-of-fit, allowing the user to prevent
 318 over-fitting of the data (the model with the lowest BIC is always preferred).

$$319 \quad BIC = \log\left(\frac{SSR}{n}\right) + \frac{K \log n}{n} \quad (11)$$

320
 321
 322 In the SOCCOM array, of the 126 floats currently considered candidates for optode drift
 323 correction, 32 exhibited significant drift rates. Both positive and negative drift rates were
 324 observed, with a mean of -0.07%/yr, a standard deviation of 0.65%/yr and a total range of -1.1 to
 325 1.2 %/yr.

326 The drift correction proposed here relies on the existence of air oxygen measurements
 327 relative to the NCEP atmospheric reference. However it does not address the root cause of
 328 sensor drift behavior which is somewhat unsatisfying. Bittig et al. (2018a) show how inadequate
 329 temperature calibration of the oxygen optode can oftentimes account for in-situ drift rates
 330 apparent in a float's optode time series. They describe a correction method (Equation 23 of
 331 referenced publication) that can simultaneously correct for inadequate temperature calibration
 332 and any seawater carryover on the sensor during sampling while in air. The supplementary
 333 material to their paper highlights the results of applying the method to UW/MBARI float 9313
 334 (WMO 5904474); the strong oxygen-temperature response exhibited by this float is shown to
 335 bias the sensor gain time series and application of the correction method effectively removes the
 336 apparent drift in sensor gain. However, recent testing demonstrates that the results of this
 337 correction are not consistent across the SOCCOM array. Fig. 5 plots computed drift in optode
 338 gain against the residual drift in optode gain after temperature compensation with Equation 23
 339 from Bittig et al. (2018a) is applied for 82 SOCCOM floats that have been operational for at least
 340 2 years. The Model II regression (shown in red) gives an offset of 0 which suggests that the
 341 Bittig et al. (2018a) correction is robust and does not add spurious drift. The slope of the Model
 342 II regression is 0.797 (different than 1 at the 99% significance level) suggesting that across the
 343 SOCCOM array, the correction reduces the apparent drift in gain by 20.3%. For certain floats,
 344 the Bittig et al. (2018a) correction tends to underestimate the magnitude of the true drift of the
 345 optode, thus, additional drift correction may be warranted. The mean difference in gain drift
 346 before versus after the correction is -0.021%/year and the standard deviation of the differences is
 347 0.31 %/yr. These results highlight the fact that the optode-temperature response is unique to each
 348 sensor. This result is in accordance with findings of Johnson et al. (2017) who show that only
 349 20% of the change in gain over time can be accounted for by temperature changes observed by a
 350 float. Such corrections should therefore not be applied systemically across the whole fleet, but
 351 rather integrated on a float-by-float basis in delayed-mode with statistical indexing to weigh the
 352 benefit of added complexity of the correction, similar to what is currently being done to assess
 353 the need for drift corrections. These methods may be integrated into the GUI framework in a
 354 similar manner in a future revision.



356
357

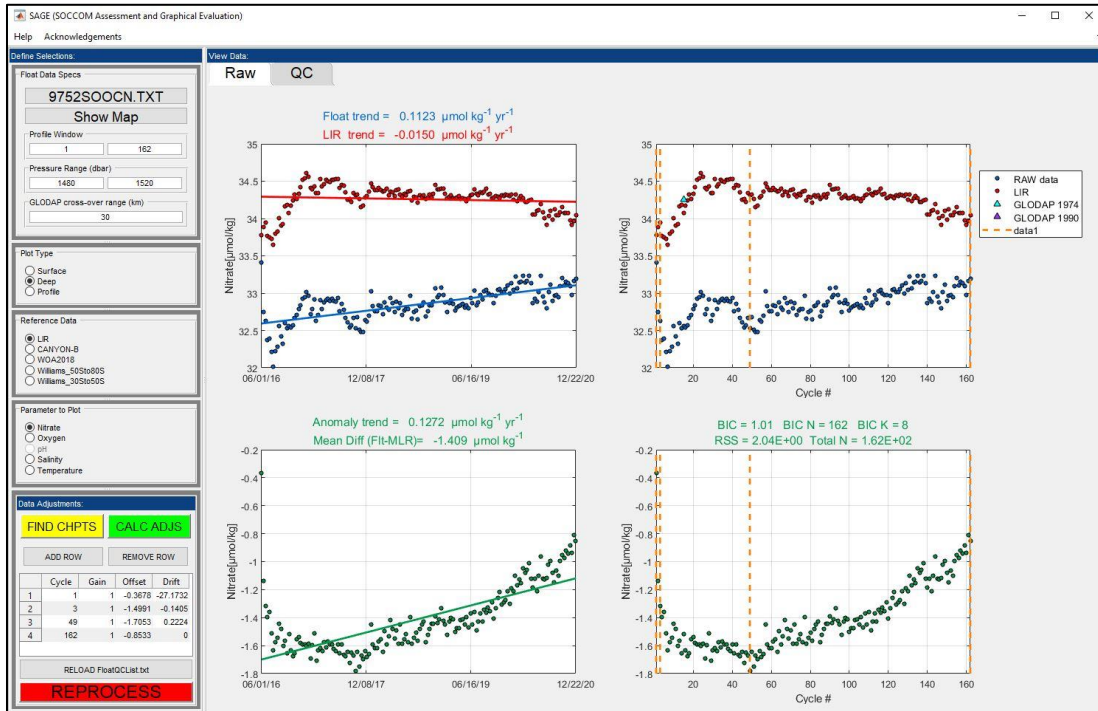
358 **Figure 5.** Comparison of post-deployment optode drift before and after application of Bittig et
359 al. (2018a) Eqn 23. Analysis includes 82 SOCCOM floats. Dashed line depicts the 1:1
360 relationship; red line is the Model II regression.

361 **4 Adjustment of nitrate and pH data**

362 Adjustment of nitrate and pH data are performed after oxygen data has been corrected.
363 Similar to oxygen optodes, nitrate and pH sensors on profiling floats often suffer from initial
364 calibration shifts that must be corrected prior to scientific use. Such inaccuracies can manifest as
365 offsets and/or drifts throughout the data series. As described in Johnson et al. (2017), pH offsets
366 and drifts can be attributed to changes to the sensor reference potential (k_0) over time, while
367 those apparent in nitrate usually result from changes in light throughput due to aging or fouled
368 optical components. Therefore, adjustments to pH and nitrate are applied as offsets to k_0 and
369 nitrate concentration [$\mu\text{mol kg}^{-1}$], respectively.

370 The general adjustment process for pH and nitrate is based on evidence that the offsets
371 and drifts are constant throughout an entire profile (Johnson et al., 2013; 2017). Corrections then
372 involve comparison of raw float data to select reference fields at depths below 1000m where
373 spatial and temporal variability in ocean chemistry is minimal. The corrections determined at
374 depth are then applied to the entire profile. This process is similar to the protocol used to correct
375 Argo salinity data (Owens & Wong, 2009). Fig. 6 below shows the SAGE GUI interface where
376 such comparisons can easily be performed. Upon selecting a float, default view specifications
377 are loaded into the GUI, including a profile window encompassing the entirety of the float's life-
378 span, and a pressure range of 1480 to 1520 m where adjustment assessment is performed. Float
379 (blue) and reference (red) data within selected time and pressure ranges are plotted in the top
380 panels, and the anomaly series (float minus reference) is plotted below in green. Global Data
381 Analysis Project v2 (GLODAPv2; Olsen et al., 2020) crossover data is also shown in the upper
382 panel plots as a climatological reference, but only to assess the consistency of adjusted data. As
383 in SAGE-O₂, the search distance for GLODAPv2 data from each profile can be set in the GUI.

384



385

386

387 **Figure 6.** SAGE GUI software interface showing raw nitrate data (blue) from MBARI/UW float
 388 9752 (WMO 5904694).

389

390 Similar to conductivity sensors (Owens & Wong, 2009), drifts and offsets occurring in
 391 data from nitrate and pH sensors often vary linearly over long time periods, and calibration
 392 jumps in the time series are not uncommon. Oftentimes the largest drift rates occur over the first
 393 few cycles in a float's life as can be seen in the nitrate anomalies shown in Fig. 6. Nitrate and
 394 pH anomalies from a float data series are thus best modeled as discontinuous piecewise linear
 395 fits, where both drifts and offsets change independently between segments that are bounded on
 396 either side by defined cycle breakpoints. In the Fig. 7 schematic, the correction, $\Delta ANOM$, at
 397 each cycle breakpoint, j , is calculated as

398

$$ANOM_j = O_j \quad (12)$$

399

400

401 and the data correction for any subsequent cycle, i , within the same segment becomes

402

$$ANOM_i = O_j + D_j(T_i - T_j) \quad (13)$$

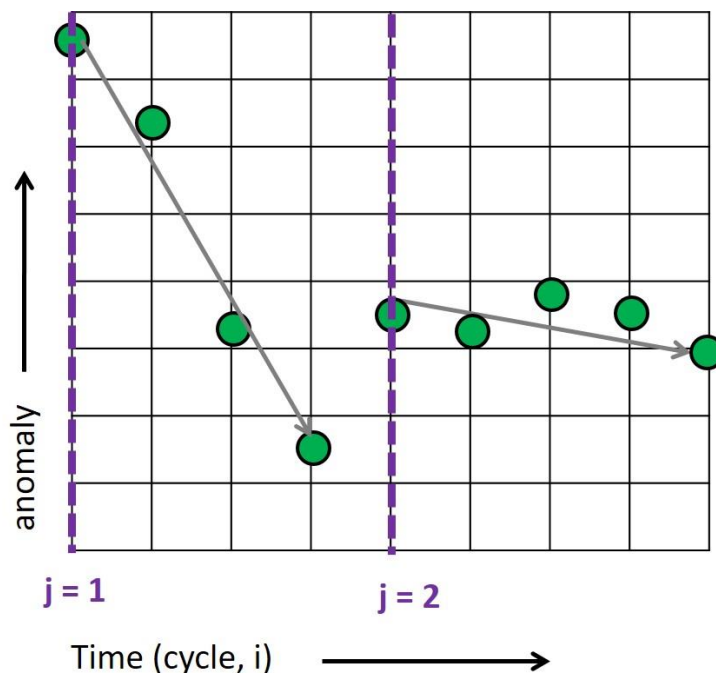
403

404

405 where O and D represent the offset (in $\mu\text{mol kg}^{-1}$) and drift (in $\mu\text{mol kg}^{-1}$ per year), respectively,
 406 of the linear least squares fit to the anomaly data series between cycles located at breakpoints j
 407 and $j+1$ (not including the latter bounding breakpoint), and T represents time (in years). For
 408 nitrate data, this modeled correction (represented by gray lines in Fig. 7) is then subtracted from
 409 the original data series. For pH data, the modeled correction is applied as an offset to the
 410 reference potential (k_0) of the sensor as described in Johnson et al. (2017). A matrix of
 411 correction factors (as shown in the lower left corner of Fig. 6) is stored in a float-specific text file

412 along with any derived oxygen corrections for use in reprocessing applications. This method
 413 constitutes a delayed-mode correction approach that can be revisited and characterized at
 414 periodic intervals throughout the float's life.

415



416

417 **Figure 7.** Qualitative schematic showing the adjustment model of a theoretical sensor anomaly
 418 series. The two series breakpoints, identified in purple, occur at cycles 1 and 5. Gray lines
 419 represent the least-squares fit (adjustment model) to the elements (green dots) within each
 420 segment.

421

4.1 Reference models for pH and nitrate

422

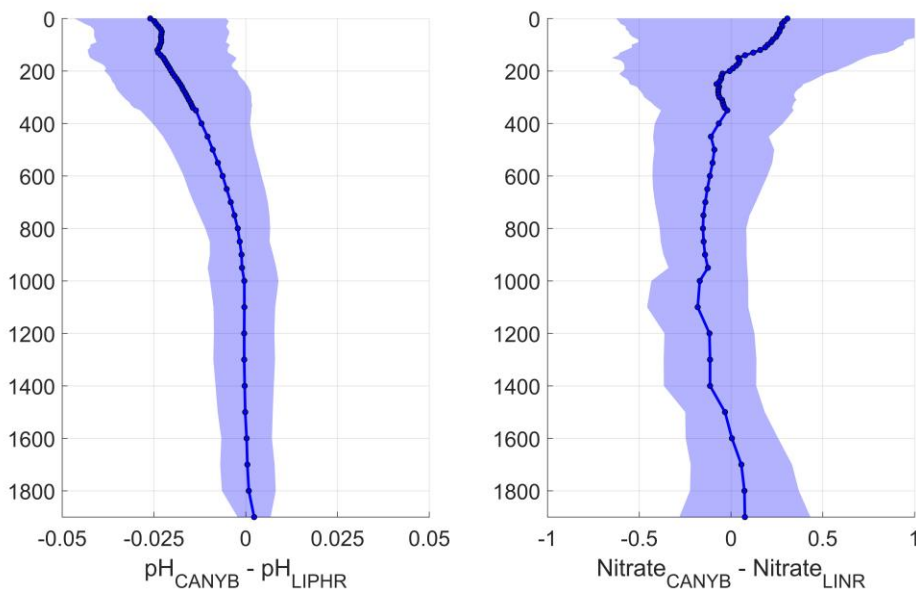
Multiple options are available for use in the estimation of deep pH and nitrate reference
 423 fields for comparison against float data. These include World Ocean Atlas climatological fields
 424 as well as empirical algorithms derived from high-quality shipboard data acquired from GO-
 425 SHIP cruises (Bittig et al., 2018b; Carter et al., 2018; Williams et al., 2016). While the
 426 algorithms provide estimated fields rather than direct measurements, their performance has been
 427 extensively validated. The set of multiple linear regression models (MLRs) by Williams et al.
 428 (2016) were the first of such reference algorithms available in the Southern Ocean and were
 429 utilized in the quality control of SOCCOM nitrate and pH float data during the early years of the
 430 program. Nitrate and pH estimates produced using the Williams method rely on MLR equations
 431 specific to two latitudinal bands around the Southern Ocean. Predictor variables include
 432 pressure, salinity, temperature, and oxygen. A key distinction between the Williams MLRs and
 433 the other methods available for use within the SAGE software is the lack of global extent in the
 434 Williams MLRs. In addition, this method is limited in depth space to the range of 1000 to 2100
 435 m. While this fully encompasses the depth nominally used in quality control for the majority of
 436 SOCCOM floats, sometimes shallower reference depths are required, for example when a float is
 437 under-ballasted and cannot reach 1000 m. Nonetheless, the Williams MLR algorithms perform
 438 very well when used within their specific range limits. Williams et al. (2016) states root mean

439 square errors (RMSE) of $0.3 \mu\text{mol kg}^{-1}$ and 0.004 total pH units for deep (1500m) nitrate and pH
440 estimates, respectively. Additionally, Johnson et al. (2017) show linear regressions between first
441 nitrate and pH profiles from SOCCOM floats, adjusted to the Williams MLRs at depth, and
442 shipboard bottle data taken at the time of deployment to be near unity, with midrange differences
443 (bottle minus float) of $-0.1 \mu\text{mol kg}^{-1}$ and 0.006 pH units, respectively. These findings are
444 important as they validate the method as an acceptable reference option for other float programs
445 in the Southern Ocean.

446 However, as increasing numbers of BGC floats are being deployed outside of the
447 Southern Ocean, an alternative reference algorithm with full global extent is now the operational
448 standard. This allows for a consistent procedure, homogenous across float arrays. The current
449 default choices for estimating nitrate and pH for comparison against SOCCOM float data are the
450 locally interpolated nitrate regression (LINR) and the locally interpolated pH regression (LIPHR)
451 (or LIRs, collectively) (Carter et al., 2018). The LIR algorithms were developed from a series of
452 MLRs trained using GLODAPv2, resulting in a separate set of coefficients for each 5 degree
453 latitude and longitude grid box and 33 different depth surfaces. The derived coefficients at each
454 grid point then get interpolated onto a float's location for use in generating a final nitrate or pH
455 estimate. As described in Carter et al. (2018), there are 16 possible groupings of predictor
456 variables available to use in producing a final estimate. For SOCCOM assessments, LIR
457 regression #7 is used with depth, salinity, temperature, and dissolved oxygen as input
458 parameters, in addition to the profile latitude and longitude. The RMSE of the residuals between
459 LIPHR and LINR estimates within 1000 and 2000m using predictor set #7 and the test
460 observations used for algorithm validation were 0.006 pH units and $0.47 \mu\text{mol kg}^{-1}$, respectively
461 (Carter et al., 2018).

462 A third optional reference algorithm is the CARbonate system and Nutrient concentration
463 from hYdrological properties and Oxygen using a Neural-network, Bayesian approach
464 (CANYON-B, Bittig et al., 2018b). This is a neural network mapping performed in a Bayesian
465 framework, that is, informed by an ensemble of model components at each stage rather than
466 fixed values. This model is a revised version of an earlier individual neural-network approach,
467 CANYON, originally developed by Sauzéde et al. (2017). In their publication, Bittig et al.
468 (2018b) compare the performance of CANYON-B with LIR for various parameters, including
469 nitrate and pH, against a post-GLODAPv2 validation dataset. The authors stress that, while both
470 methods perform similarly well in a bulk statistical sense, local estimates can still be quite
471 different. Fig. 8 compares differences between pH and NO_3^- estimates for the SOCCOM array
472 using CANYON-B and LIR algorithms. The mean (standard deviation) of the differences at the
473 depth that QC is performed within SAGE are -0.001 (0.006) for pH and -0.053 (0.278) $\mu\text{mol kg}^{-1}$
474 for NO_3^- . Larger differences near the surface are largely due to greater uncertainties of the LIR
475 algorithms at these depths (although, as noted by Bittig et al., (2018b), estimates from all
476 algorithms show some level of enhanced uncertainty toward the surface due to difficulty in
477 accurately capturing seasonal variability and effects of air-sea gas exchange). The enhanced skill
478 in near-surface depths exhibited by CANYON-B, relative to LIR, can serve as an independent
479 validation to the calibration approach. Surface data from floats corrected at depth using LIR
480 frequently align well with CANYON-B estimates at the surface, in a qualitative sense. However,
481 it should be noted that pH estimates generated by CANYON-B are intended to be in line with pH
482 calculated from DIC and TA, rather than pH that has been spectrophotometrically measured,
483 whereas pH measurements using the LIPHR method are the opposite. While the LIPHR

484 algorithm has a flag to apply a linear adjustment that will subsequently produce estimates
 485 consistent with calculated pH, this method should not be used for calibrating a pH measurement
 486 from a float, as ISFET pH is consistent with spectrophotometric pH measurements (Takeshita et
 487 al., 2020). The differences shown in Fig. 8 were performed after a linear transformation was
 488 applied to CANYON-B estimates following Carter et al. (2018) (Equation 1) to bring estimates
 489 back into alignment with spectrophotometrically measured pH.



490
 491 **Figure 8.** Fleet-wide differences of computed pH (left) and nitrate (right) using CANYON-B and
 492 LIR algorithms. Data were binned at 10, 50 and 100m pressure intervals for 0-350, 350-1000,
 493 and 1000-2000 db, respectively. The blue line represents the mean difference and the shaded
 494 areas represent +/- 1 standard deviation.

495 A final note should be made regarding the use of pH estimates that are based on
 496 measurements made over a large time span. Ocean pH is decreasing due to increasing
 497 atmospheric carbon dioxide concentrations and these effects are sometimes detectable at the
 498 depth range used for pH sensor adjustment (Rios et al., 2015). Each of the algorithms described
 499 here has been trained on shipboard data that may exhibit this effect. While the LIPHR algorithm
 500 does include a flag for optional application of an ocean acidification adjustment, this is a static
 501 adjustment and does not account for geographic differences in ocean acidification rates, nor does
 502 it account for changes in global ocean acidification rates over time. This highlights the need for
 503 such reference equations to be periodically updated, utilizing recent training datasets to provide
 504 more accurate algorithm coefficients.

505 4.2 Computation of correction factors using automated change-point detection

506 In the initial version of the SAGE software, the user manually chose the location of each
 507 breakpoint (node). The inherent subjectivity in this approach in addition to the increasing time
 508 investment required by the operator to complete a full adjustment assessment of the SOCCOM
 509 array proved less than optimal. In the current software version, both the optimal number and
 510 location of each breakpoint can be assigned automatically through an automated multi-step

511 process. First, the binary segmentation method of change-point detection is applied using the
 512 MATLAB function, `ischange`, which begins by splitting the data series for variable y , of length
 513 n , into two segments separated by a change-point, j (Killick et al., 2012). The location of j along
 514 the time series is then iteratively shifted until a minimization of the left side of the following
 515 equation is reached:

$$516 \quad C(y_{1:j}) + C(y_{(j+1):n}) < C(y_{1:n}) \quad (14)$$

517
 518 where C represents the cost function

$$519 \quad C(x) = n\text{Var}(x) \quad (15)$$

520
 521 where n is the number of data points in the segmented data series, x , and Var is the variance.
 522 This process is then repeated, further splitting up the segments to find the optimal location of an
 523 increasing number of changepoints. Next, in order to statistically determine the best number of
 524 changepoints of the various groupings tested, a modified BIC is calculated for each model,
 525 following

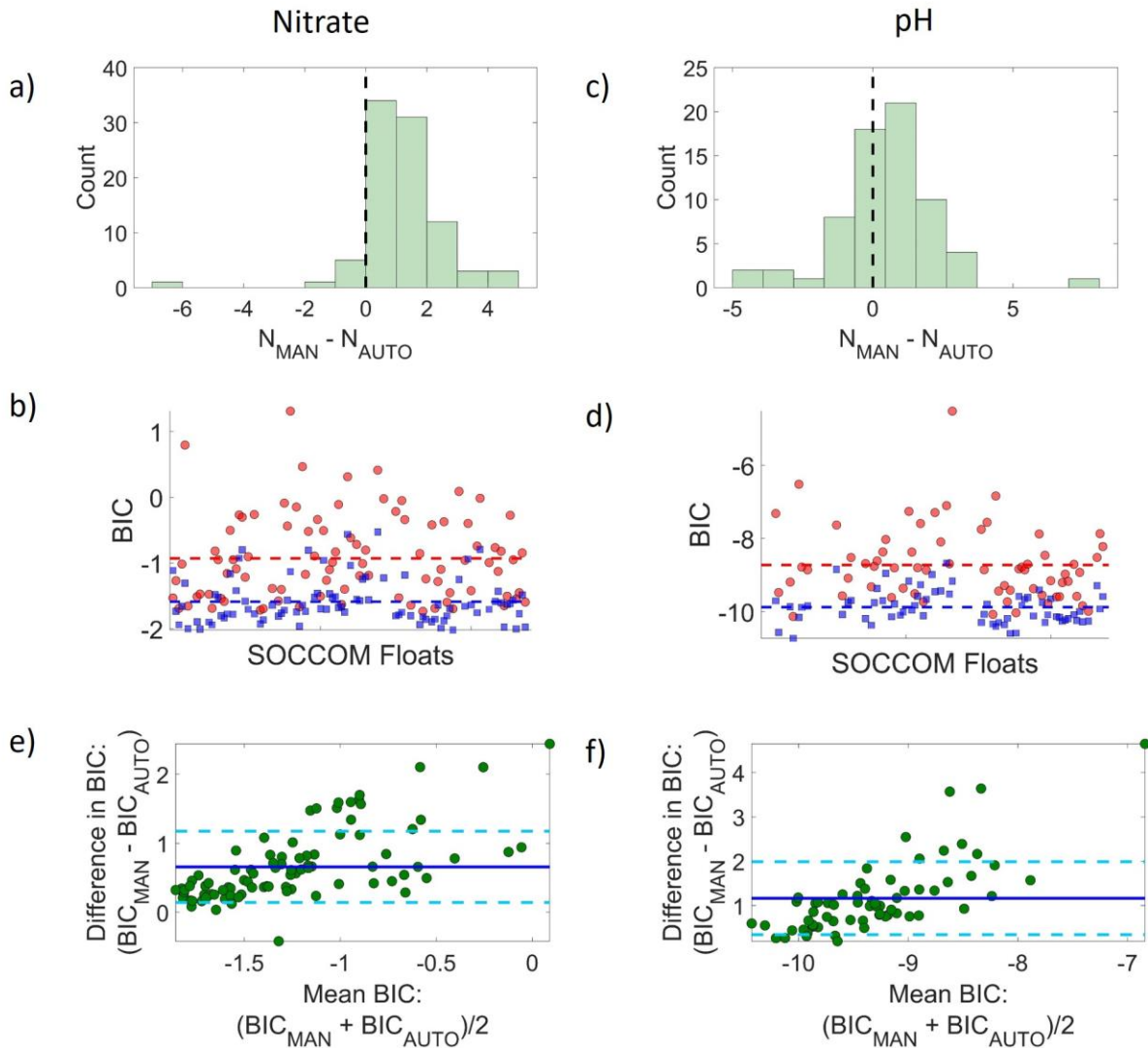
$$526 \quad BIC = \log\left(\frac{SSR}{n} + \alpha^2\right) + \frac{K \log n}{n} \quad (16)$$

527
 528 where the α term is used as a threshold on the mean residual, driven by the basic precision of the
 529 sensor. In SOCCOM processing operations, $\alpha=0.5$ (0.005) is used for nitrate (pH) data. If α is
 530 omitted, equivalent to assuming the sensor has no inherent noise, the changepoint algorithm will
 531 often find an excessive number of change points, which is inconsistent with known sensor
 532 behavior. The location and number of changepoints from the model with the lowest BIC value is
 533 then used to derive offsets and drifts as described in Section 4.

534 A key concern in the move from a manually-assigned to an automated definition of
 535 breakpoints in the sensor QC process was to maintain the final quality of the adjusted SOCCOM
 536 dataset. Thus, prior to operational implementation of the automated method, a quality
 537 assessment was performed using two adjusted datasets, one done manually by a trained
 538 biogeochemical float quality control operator and the other performed automatically using the
 539 changepoint detection method described above. Fig. 9 (a-d) shows that the use of automated
 540 changepoint detection in the SOCCOM QC process results in a fewer number of change-points,
 541 on average, and an overall better model of the anomaly time series, in a statistical sense (lower
 542 BIC value), than the previously employed manual correction method.

543 However, the absolute difference in BIC between models is small in most cases (mean
 544 differences of 0.658 and 1.165 for nitrate and pH, respectively) with the automated method
 545 showing progressively better performance as model complexity increases (Fig. 9, e-f). It is
 546 generally accepted that when comparing candidate models, a difference in computed BIC less
 547 than 2 is relatively inconsequential, meaning that the two models are statistically similar and
 548 minimal (if any) improvement can be attained by choosing one over the other (Fabozzi et al.,
 549 2014; Kass & Raftery, 1995). When taken in this context, results from this comparison suggest
 550 that the initial manual method of change-point detection for QC across the SOCCOM fleet was
 551 not of poor quality, and that the move to automated changepoint detection sustains such quality
 552 while concurrently reducing the time required to perform an objective fleet-wide assessment.

557

558
559

560 **Figure 9.** (a,b): Histograms showing differences in number of changepoints identified by the
 561 manual (N_{MAN}) versus automated (N_{AUTO}) method for nitrate and pH sensor QC. (c,d):
 562 Comparison of computed Bayesian Information Criterion (BIC) for manual (red circles) and
 563 automated (blue squares) changepoint identification in nitrate and pH QC. Dashed lines represent
 564 mean BIC values for each method. (e,f): Difference in computed BIC (manual versus auto)
 565 against mean BIC value for each float, for nitrate and pH. Solid and dashed lines represent mean
 566 difference ± 1 standard deviation, respectively. 120 SOCCOM floats were used in each
 567 analysis.

568 4.3 pH and nitrate adjustments in the SOCCOM array

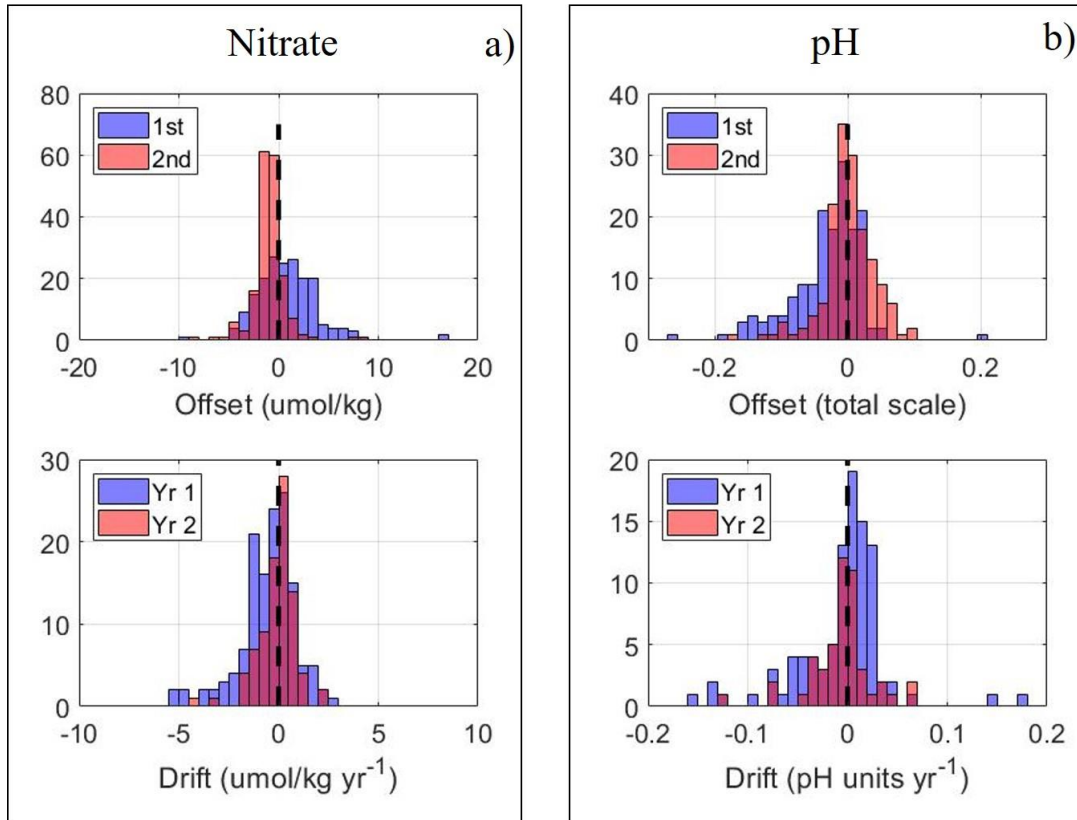
569 The magnitude of a required sensor adjustment, as derived from the methods described in
 570 the previous sections, represents the degree to which sensor performance has changed since
 571 laboratory calibration. A summary of the adjustments required over time across a full array of

572 sensors can unveil any systematic biases and subsequently help identify key areas for which to
573 focus future development efforts. While the adjustment methods described in this paper improve
574 data accuracy, reducing the magnitude of required adjustments to a sensor is the optimal goal.
575 As described in Section 4, the coefficients to the linear fits of each segmented anomaly series are
576 included within a single float-specific correction matrix that is used in the data adjustment
577 process. The offset associated with the first segment exemplifies sensor performance upon
578 deployment. As each segment is treated independently, the value of any subsequent offset can
579 provide information on sensor health over time when viewed relative to the first offset.

580 The distributions of the first and second offsets required for nitrate and pH data in the
581 SOCCOM array are shown in Fig. 10. The positive skew of the nitrate first offset distribution
582 demonstrates that the majority of SOCCOM nitrate sensors are biased high upon deployment
583 while the opposite is true for pH sensors within the array. The magnitude of the bias is 0.91
584 $\mu\text{mol kg}^{-1}$ for nitrate, and -0.032 for pH (Table 2). Distributions of the second offsets (relative
585 to the first) show reduced spread across both sensor types and an elimination of bias in pH sensor
586 data. This behavior is not surprising; oftentimes the largest anomaly is observed on the first
587 cycle as the sensor re-conditions to an aqueous environment. Continued exposure to seawater at
588 1500m helps to stabilize the sensors, particularly the pH sensor. The optics of the nitrate sensor
589 are more sensitive to perturbations so jumps in the data series are more often observed. This is
590 exemplified by the fact that a small bias (negative) remains in the distribution of second nitrate
591 offset, showing that a second offset is almost always required to bring nitrate data in line with
592 climatology.

593 Also notable in the distributions is that there is a small subset of floats receiving
594 relatively large first offset corrections for nitrate and pH sensor data. Currently there is no
595 operational threshold in place for maximum allowable adjustment. Floats requiring larger than
596 normal nitrate or pH adjustments are analyzed on a case-by-case basis and may be grey-listed as
597 bad or questionable by the delayed-mode operator upon review of laboratory calibration and
598 sensor diagnostics. These large offsets may be the result of changes in optical alignment or
599 sensor contamination during transport.

600
601

602
603

604 **Figure 10.** Histograms of first and second offsets (top), and first-year and second-year drift rates
 605 (bottom) for nitrate (a) and pH (b) data. Offsets were computed as float data minus reference
 606 data at a nominal calibration depth of 1500m; the second offset is relative to the first. Drift rates
 607 were computed using a Model I regression on the anomaly time series.

608

a)	Nitrate 1 st offset ($\mu\text{mol kg}^{-1}$)	Nitrate 2 nd offset ($\mu\text{mol kg}^{-1}$)	Nitrate 1 st -year drift ($\mu\text{mol kg}^{-1} \text{yr}^{-1}$)	Nitrate 2 nd -year drift ($\mu\text{mol kg}^{-1} \text{yr}^{-1}$)
Median	0.72	-0.95	-0.17	0.08
Mean	0.91	-0.95	-0.51	-0.09
Std dev	3.12	1.75	1.52	0.96

609

b)	pH 1 st offset	pH 2 nd offset	pH 1 st -year drift (yr^{-1})	pH 2 nd -year drift (yr^{-1})
Median	-0.020	0.002	0.000	-0.002
Mean	-0.032	0.001	-0.017	-0.005
Std dev	0.059	0.040	0.060	0.032

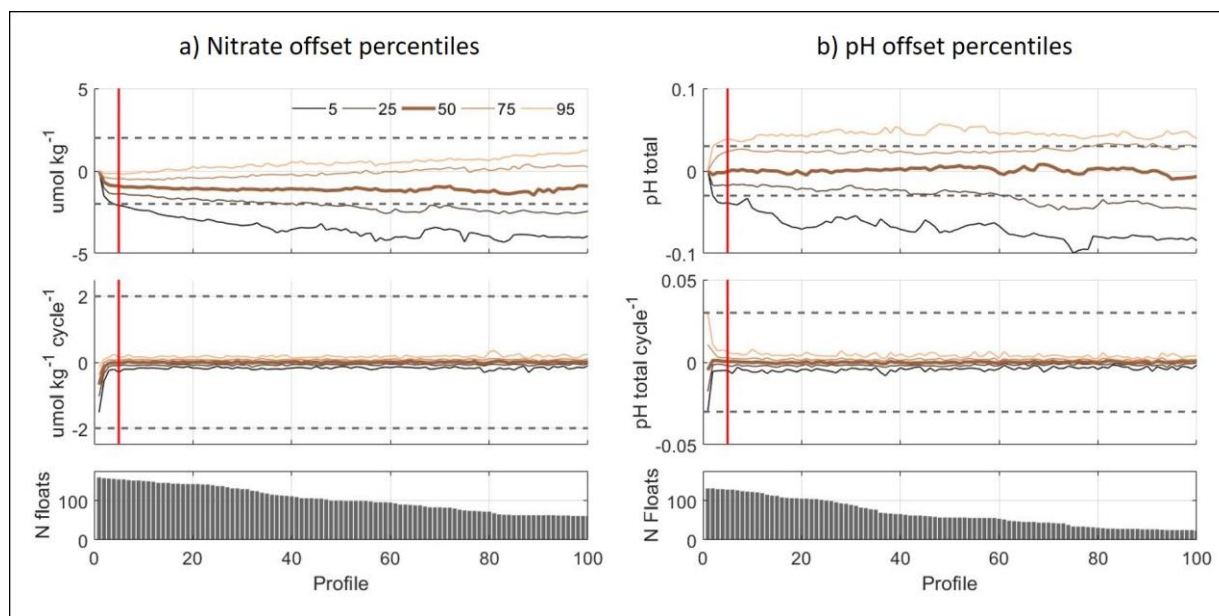
610

611 **Table 2.** Data adjustment summary statistics for nitrate (a) and pH (b).
 612

613

614 First year and second year sensor drifts for nitrate and pH are also shown in Fig. 10
 (lower histograms). These were computed as the slope of a Model I regression over the first and

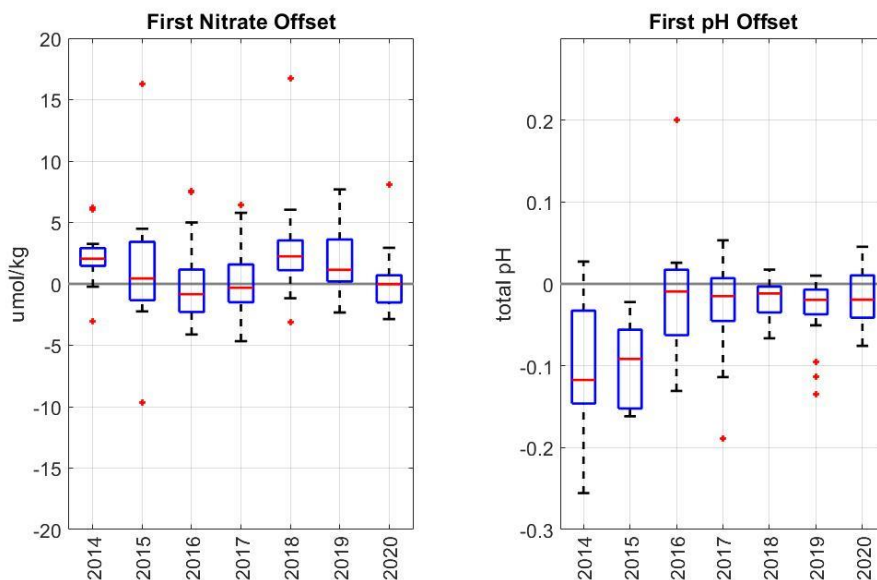
615 second year of data for each float. This ensured a uniform time frame for drift comparison
 616 across the array (as the length of each segment within a float's adjustment matrix can vary).
 617 While drift in the second year is not completely eliminated, there is an 80% (70%) reduction in
 618 mean drift rate across the array for nitrate (pH) sensors from year 1 to year 2. The reduction in
 619 sensor drift from year 1 to year 2 is not a uniform rate of change. This can be seen in Fig. 11 that
 620 shows percentiles across the array of computed anomalies at each profile relative to that of the
 621 first profile (top) and percentiles of the rate of change in anomaly by profile (center). By the
 622 second year, around 25% of nitrate anomalies have drifted beyond $2 \mu\text{mol kg}^{-1}$ of their initial
 623 value with the majority of sensors drifting negative (measuring low relative to reference fields)
 624 and the largest proportion of drift occurring within the first five cycles (red line). pH sensors see
 625 both positive and negative drift rates, with close to 50% of the data drifting beyond 0.03 pH units
 626 of their initial value. However, similar to nitrate sensors, pH sensors are also relatively stable
 627 beyond the first few cycles. Because both nitrate and pH sensors exhibit the largest rates of in
 628 situ drift within the first 2 months since deployment, it is recommended that initial QC
 629 assessment be performed only after the first 5 cycles have been returned from a float.
 630
 631



632
 633 **Figure 11.** Nitrate (a) and pH (b) offset percentiles. Offsets are computed as the anomaly (float
 634 – reference) at each profile across the array. Top panels display offsets relative to profile one;
 635 center panels display the rate-of-change (first derivative) in offset from profile to profile
 636 (SOCCOM floats cycle at 10-day intervals); lower panels show the number of floats at each
 637 profile number.

638 While we see sensor stability improving with time since deployment for individual
 639 sensors, it is also important to understand if adjustment requirements across the array are
 640 improving over each subsequent deployment year. Fig. 12 shows box plots of the first offsets
 641 required for nitrate (left) and pH (right) data grouped by deployment year. Median offsets for
 642 nitrate seem to be more or less randomly distributed around zero. For pH, this is not the case.
 643 Median values remain negative over all deployment years which suggests a systematic negative
 644 bias for this sensor. pH sensor offset statistics also show a more dramatic change over time, in

645 both the location of central tendency and degree of dispersion. These shifts in offset statistics are
 646 likely linked to changes in sensor design or laboratory calibration procedure. For example,
 647 significant improvements were seen in 2016 and 2018 in conjunction with the move to a thicker
 648 ISFET covering, and the switch from silver to platinum wire connections on the ISFET
 649 electrode, respectively. Beginning in 2016 the offset distributions are centered closer to zero
 650 than in previous years, and the 2018 distribution has a much tighter interquartile range,
 651 indicating more consistent sensor behavior.
 652



653

654 **Figure 12.** Boxplot summaries of first nitrate (left) and first pH (right) offsets, grouped by
 655 deployment year. Red lines represent the median, box boundaries represent the interquartile
 656 range ($Q3 - Q1$), whiskers are the outer range of data, excluding outliers (red stars) which are
 657 defined as data points that are larger than $Q3 + 1.5 * (Q3 - Q1)$ or smaller than $Q1 - 1.5 * (Q3 - Q1)$.

658 5 Validating SOCCOM float data adjustments

659 In this section, we discuss a system for validating our calibration methods. This involves
 660 comparison of post-corrected float data to data from both high-quality shipboard bottle casts
 661 taken alongside each SOCCOM float at the time of deployment, and nearby stations within the
 662 GLODAPv2 dataset (Olson et al., 2020). While shipboard data can also be useful for assessing
 663 initial offsets along a profile, it is not essential to float calibration and is typically reserved as an
 664 independent validation of the employed correction methods.

665 5.1 The use of shipboard bottle data

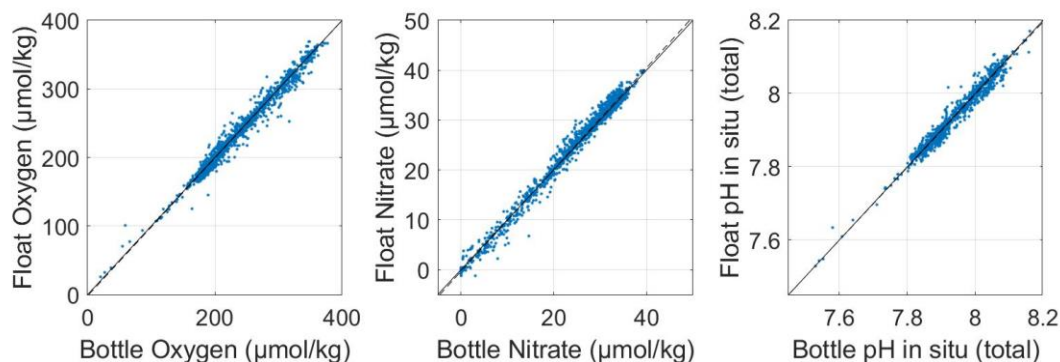
666 With the exception of oxygen calibration on Navis floats, the methods described in the
 667 previous sections for adjusting chemical data from a float do not depend on the existence of
 668 shipboard reference data collected alongside a float's deployment. This is advantageous in that
 669 any shipboard data taken at the time of deployment can be used to validate the applied in situ
 670 calibration methods. The SOCCOM program has required shipboard data collection alongside
 671 float deployment wherever possible to support the building of a robust validation dataset.

672 However, because it is not essential to sensor quality control, shipboard data collection may be
 673 reduced to select cruises in the future.

674 Comparisons of SOCCOM quality-controlled float data against shipboard data taken near
 675 the time of deployment are shown in Figs. 13 and 14. All float data have been interpolated onto
 676 the pressure axis of the hydrocast data. A portion of the error in the differences can be attributed
 677 to spatial and temporal changes in hydrography between the float profile and bottle samples.
 678 Float deployments typically occur as the ship begins heading away from a sampling station after
 679 the CTD rosette cast has been performed. This is done to reduce the chances of the ship running
 680 into the float. An additional lag time exists between deployment and when the float completes
 681 its first profile. Float-to-bottle matchups in the SOCCOM array are on average 23 hours and 8
 682 km apart in time and space because of this. Nonetheless, the float to bottle matchups show very
 683 good agreement. The slope of the Model II regression for each parameter is indistinguishable
 684 from the 1:1 line. The median bottle-minus-float difference for oxygen, nitrate and pH are 0.35
 685 $\mu\text{mol kg}^{-1}$, $-0.12 \mu\text{mol kg}^{-1}$, and 0.002 total pH units, respectively (Table 3). These values are
 686 very close to the accuracies reported in Johnson et al. (2017). Oxygen shows the largest
 687 improvement; this can likely be attributed to the implementation of the optode drift correction
 688 which was not yet accounted for at the time of the Johnson et al. (2017) publication.

689 Additionally, an independent analysis by Mignot et al. (2019) of quality controlled BGC-
 690 Argo float data in the Mediterranean Sea shows similar results, stating accuracies for oxygen and
 691 nitrate data (when compared to shipboard measurements) of 2.9 and 0.46 $\mu\text{mol kg}^{-1}$, respectively.
 692 Maximum depths reached by floats in the Mignot et al. (2019) analysis was 1000 m, as opposed
 693 to 2000 m on SOCCOM floats. The upper water column, therefore, made up a larger relative
 694 proportion of their float-to-bottle dataset; spatio-temporal mismatch due to greater oceanic
 695 variability at these depths likely accounts for the slightly larger biases observed.

696



697

698

699 **Figure 13.** Scatter plots of float oxygen (left), nitrate (middle) and pH (right) data versus
 700 shipboard bottle data. The solid and dashed lines represent the 1:1 and Model II least squares fit,
 701 respectively.

702

703

704

705

706

707

708

709

	N observations	mean	median	standard deviation	maximum	minimum
Oxygen ($\mu\text{mol kg}^{-1}$)	2366	0.94	0.35	6.84	64.50	-41.82
Nitrate ($\mu\text{mol kg}^{-1}$)	2240	-0.22	-0.12	1.00	7.89	-5.14
pH (in-situ total)	1145	0.002	0.002	0.015	0.061	-0.096

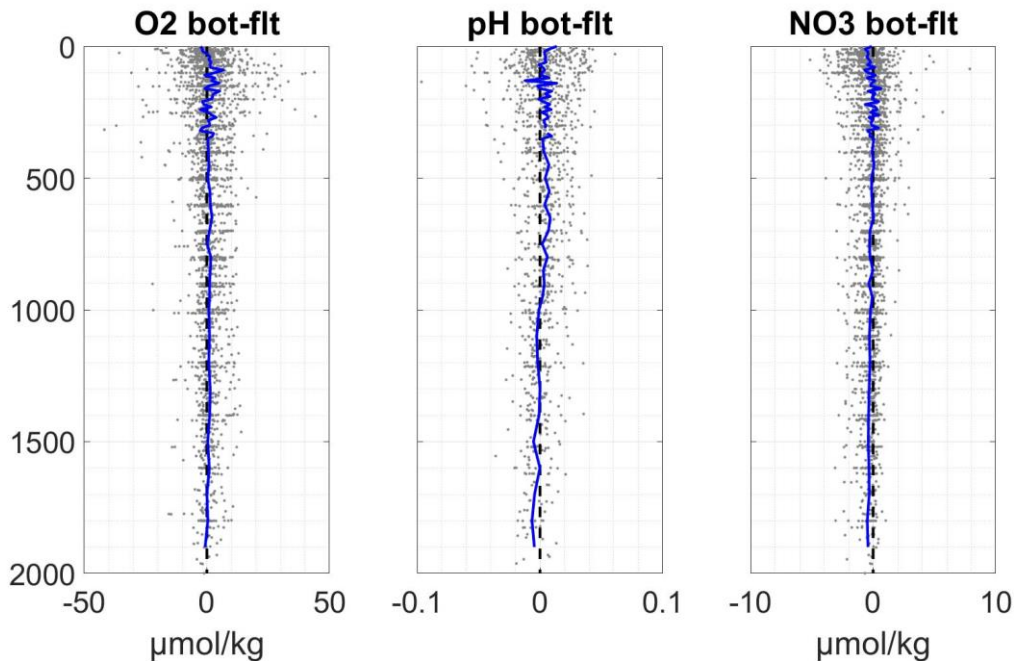
710

711 **Table 3.** Bottle – minus – float matchup summary statistics for oxygen, nitrate and pH.

712

713 Float-bottle matchups in pressure space provide a validation of the assumption that sensor
 714 offsets are constant with depth (Johnson et al., 2013; 2016; 2017). Fig. 14 shows the bottle-
 715 minus-float differences for all oxygen, pH and nitrate matchups, plotted against pressure. The
 716 blue lines represent binned averages. There are no large trends in the oxygen or nitrate values
 717 with depth, confirming the assumptions in our calibration method. For pH, the pressure-binned
 718 distribution of mean differences show a negative bias of 5 millipH at depth. This bias changes
 719 sign toward the surface. Johnson et al. (2016) show a similar trend in comparison to discrete
 720 data (Fig. 6 in their publication, note trend is reversed as their plot represents float-minus-
 721 discrete) which they attribute to an incomplete understanding of carbonate-system
 722 thermodynamics at high pressures. While the magnitude of this bias is within the limits of stated
 723 uncertainty in the pH correction method (see section 4.2), the depth-dependent nature of the pH
 724 bias, as evident in the data, should be researched further.

725



726

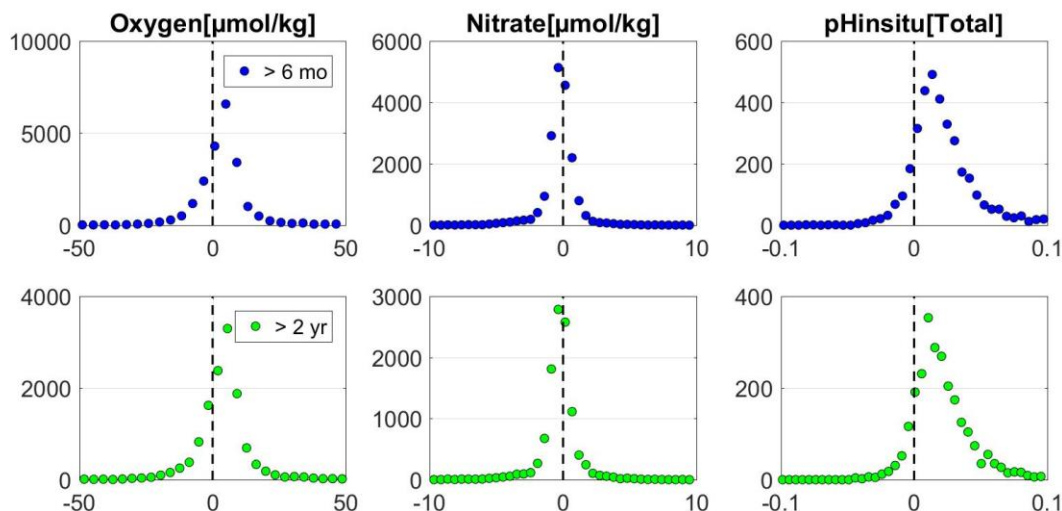
727

728 **Figure 14.** Scatterplots of bottle minus float matchups for oxygen (left), pH (center) and nitrate
 729 (right) data, plotted in depth space. Blue lines represent the mean of data within depth bins.

730 5.2 Comparisons to GLODAPv2

731 As described in the previous section, SOCCOM data quality validation is performed
732 primarily in reference to shipboard hydrographic data taken at the time of deployment and is thus
733 limited in scope to the initial profile returned from each float. Since in-situ drift is often
734 observed in nitrate and pH (and to a lesser degree, oxygen) sensors onboard SOCCOM floats, a
735 logical question is whether or not the quality of the applied adjustments remains stable
736 throughout the duration of a float's life. For nitrate and pH, degradation in the quality of the
737 adjustment over time could come from either a reduction in accuracy in one of the input
738 parameters to the reference models (namely, temperature, salinity or oxygen), or a reduction in
739 the accuracy of the reference algorithm itself due to gradual changes in deep ocean conditions
740 that challenge the validity of the empirical relationships. The first possibility poses less of a
741 threat, as temperature and salinity data on Argo floats are quite stable and require minimal
742 adjustment. And, although drift is observed in some optodes onboard SOCCOM floats (see
743 Section 3.2), comparison to a stable atmospheric reference provides a robust means for
744 correction. The potential for degradation in data adjustment quality through time due to changes
745 in the pressure or temperature coefficients of the sensor is more of a concern. If such changes in
746 calibration occurred, then corrections derived at depth as the sensor aged would not be accurate
747 near the surface.

748 The impacts from the issues described in the preceding paragraph can be assessed for the
749 current SOCCOM dataset through an independent comparison of SOCCOM quality-controlled
750 data at different stages of a float's life with hydrographic data from nearby stations in the
751 GLODAPv2 dataset (Olson et al., 2020). Fig. 15 shows histograms of GLODAPv2 minus float
752 data for oxygen, nitrate and pH crossovers within 20km distance of GLODAPv2 station data
753 with no temporal restrictions; only data below 300 dbar were used to minimize discrepancies due
754 to seasonal variability in the upper water column. The upper panels in the figure include
755 comparisons from floats older than 6 months of age, and the lower panel includes data from
756 floats greater than two years of age. A $4 \mu\text{mol kg}^{-1}$ and 0.02 pH bias between float and
757 GLODAPv2 data can be observed for oxygen and pH data, respectively. The consistency of the
758 biases for young (< 6 months) and old (> 2 years) floats are thus more likely a result of temporal
759 differences between mean GLODAPv2 data used in the analysis and the corrected SOCCOM
760 dataset. The mean age difference between the two datasets is 17.8 years. A $4 \mu\text{mol/kg}$ decrease
761 in oxygen over nearly two decades ($0.2 \mu\text{mol/kg/y}$) is consistent with reported rates of oxygen
762 change in the Southern Ocean that are based on shipboard data (Helm et al., 2011). Additionally,
763 the observed rate of change in pH across this time frame (0.001 pH/y) is consistent with expected
764 and observed rates of ocean pH decrease due to increasing atmospheric CO_2 (ocean acidification;
765 Rios et al., 2015; Williams et al., 2018). Further, as is shown in Johnson et al. (2017), both the
766 oxygen and pH biases increase with the mean age difference between the GLODAPv2 station
767 time and the profiling float measurement time. This lends support to our hypothesis that the
768 biases for oxygen and pH seen in Fig. 15 are the result of dynamic ocean change in the Southern
769 Ocean in response to global climatic shifts (Bronse laer et al., 2020). This provides strong
770 evidence that the quality control methods continue to be accurate over the lifetime of the float.



771

772 **Figure 15.** Histograms of GLODAPv2 minus quality-controlled oxygen (left), nitrate (center)
 773 and pH (right) float data. Upper panels include data from floats older than six months of age;
 774 lower panels include data from floats older than two years of age. Matchups were restricted to
 775 data that was within 20 km of GLODAPv2 reference stations.

776 6 Discussion and Conclusions

777 In this paper, we presented a coherent framework for applying delayed-mode adjustment
 778 procedures to oxygen, nitrate and pH data from SOCCOM biogeochemical profiling floats. The
 779 software GUIs presented, SAGE (SOCCOM Assessment and Graphical Evaluation) and SAGE-
 780 O₂, provide a robust way to visualize and assess the quality of these data. These software are
 781 open source and available through GitHub ([https://github.com/SOCCOM-](https://github.com/SOCCOM-BGCArgo/ARGO_PROCESSING)
 782 [BGCArgo/ARGO_PROCESSING](https://github.com/SOCCOM-BGCArgo/ARGO_PROCESSING)). The tools are intended to be used periodically throughout a
 783 float's life to reexamine sensor performance in delayed-mode. Adjustments derived using the
 784 software can then be applied to existing data and propagated forward in real-time until the next
 785 delayed-mode assessment is completed. A notable aspect of the procedure is in the relationship
 786 between the oxygen adjustment and that of nitrate and pH. The collective use of both SAGE-O₂
 787 and SAGE offers a clear pathway to adjusted data for oxygen optodes, nitrate and pH sensors, all
 788 of which commonly coexist on biogeochemical profiling float platforms.

789 The successful expansion of the BGC-Argo program on a global scale, as described by
 790 Roemmich et al. (2019), depends partially on the implementation of standardized data
 791 adjustment methods across float platforms. The SAGE tools have already been adopted for use
 792 by other Argo data centers and are helping to increase the level of high-quality biogeochemical
 793 profiling float data available to users around the world. Although these software were developed
 794 specifically for the SOCCOM program, output files can be transformed to Argo NetCDF format
 795 via a separate processing pathway. Structuring the tools in this way has allowed for flexibility in
 796 adaptation across data centers. Additionally, this flexibility means that applications are not
 797 limited to Argo float data. The SAGE tools have the potential for use in post-deployment
 798 calibration of nitrate and pH data from other platforms such as gliders as well (Takeshita et al.,
 799 2020). As Bushinsky et al. (2019b) describe, sustaining multiple types of observational
 800 platforms in the ocean can increase our ability to resolve key processes at different spatial and
 801 temporal scales and in regions particularly susceptible to the effects of global change such as

802 coral reef habitats and coastal upwelling zones. Ensuring that biogeochemical data is
803 comparable across platforms is therefore essential.

804 Furthermore, along with performing repeated, standardized QC procedures it is important
805 to run validation analysis, as described in Section 5, with regularity. This provides a metric for
806 tracking improvements to sensor accuracy over time and testing the effects of processing
807 upgrades or changes in QC methodology on the quality of the dataset. While data from
808 biogeochemical sensors onboard profiling floats are revolutionizing capabilities in global ocean
809 carbon research and modeling (Ford, 2020), the operational limitations of the sensors and the
810 measurements they provide cannot be overlooked. Characterizing the uncertainties associated
811 with such measurements helps to identify gaps in our understanding and guide future research
812 and development. It is our hope that the calibration methods applied within the SOCCOM
813 program, as outlined above, will serve as a global model for profiling float quality control, but
814 also that the validation that follows will help to constrain the scientific questions that can be
815 asked and provide inspiration for future research in both chemical sensor development and
816 quality control.

817 **Acknowledgments, Samples, and Data**

818 All float data were collected and made freely available by the Southern Ocean Carbon and
819 Climate Observations and Modeling (SOCCOM) project funded by the National Science
820 Foundation, Division of Polar Programs (NSF PLR-1425989, with extension NSF OPP-
821 1936222), supplemented by NASA, and by the International Argo Program and the NOAA
822 programs that contribute to it. The Argo Program is part of the Global Ocean Observing System
823 (<https://doi.org/10.17882/42182>, <https://www.ocean-ops.org/board?t=argo>). Additionally, all
824 data analysis and supporting work performed at the Monterey Bay Aquarium Research Institute
825 was supported in part by the David and Lucile Packard Foundation. The comparison in Section
826 4.2 was done using SOCCOM data archives <https://doi.org/10.6075/J0QJ7FJP>
827 and <https://doi.org/10.6075/J01GOJKT>. Float data used for analysis in all other sections can be
828 found at <https://doi.org/10.6075/J0B27ST5>. Raw msg files returned from SOCCOM floats are
829 also freely available at <ftp://ftp.mbari.org/pub/SOCCOM/RawFloatData/combined/>. Shipboard
830 data used in validation of SOCCOM float data is available through CCHDO
831 (<https://cchdo.ucsd.edu/search?q=soccom>). World Ocean Atlas data used in this study can be
832 found at <https://www.ncei.noaa.gov/data/oceans/woa/WOA18/>. GLODAPv2 data used in this
833 study can be found at <https://www.glodap.info/index.php/merged-and-adjusted-data-product/>.
834 NCEP Reanalysis data was provided by the NOAA/OAR/ESRL PSL, Boulder, Colorado, USA,
835 from their Web site at <https://psl.noaa.gov/>. We would like to thank all people who contributed
836 to the production, calibration and assembly of all sensors and floats used within the SOCCOM
837 program, as well as all personnel involved in their transport and deployment at sea. We
838 gratefully acknowledge contributions provided by Yui Takeshita and Annie Wong during the
839 initial revision of the manuscript. We would also like to thank MBARI intern, Tatiana Ellis, for
840 her contributions to the testing of automated change-point-detection within the SAGE GUI
841 framework. MATLAB code for the SAGE and SAGE-O₂ software tools is freely available at
842 https://github.com/SOCCOM-BGCArgo/ARGO_PROCESSING/ (release 2.0).

843

844 **References**

- 845 Aanderaa Instruments. (2017), TD269 Operating Manual, oxygen optode 4330, 4831, 4835,
846 Seventh Ed.
847
- 848 Benson, B. & Krause, D. (1984), The concentration and isotopic fractionation of oxygen
849 dissolved in freshwater and seawater in equilibrium with the atmosphere. *Limnology and*
850 *Oceanography*, 29: 620-632.
851
- 852 Bianchi, D., Dunne, J. P., Sarmiento, J. L., & Galbraith, E. D. (2012), Data-based estimates of
853 suboxia, denitrification, and N₂O production in the ocean and their sensitivities to dissolved
854 O₂. *Global Biogeochemical Cycles*, 26, GB2009, doi:10.1029/2011GB004209
855
- 856 Bittig, H. C., Fiedler, B., Scholz, R., Krahnemann, G., & Körtzinger, A. (2014), Time response of
857 oxygen optodes on profiling platforms and its dependence on flow speed and
858 temperature. *Limnology and Oceanography: Methods*, 12, doi: 10.4319/lom.2014.12.617.
859
- 860 Bittig, H.C., & Körtzinger, A. (2015), Tackling Oxygen Optode Drift: Near-Surface and In-Air
861 Oxygen Optode Measurements on a Float Provide an Accurate in Situ Reference. *Journal of*
862 *Atmospheric and Oceanic Technology*, 32, 1536–1543, [https://doi.org/10.1175/JTECH-D-14-](https://doi.org/10.1175/JTECH-D-14-00162.1)
863 [00162.1](https://doi.org/10.1175/JTECH-D-14-00162.1)
864
- 865 Bittig, H. C., & Körtzinger, A. (2017), Technical note: update on response times, in-air
866 measurements, and in situ drift for oxygen optodes on profiling platforms. *Ocean Science*. 13, 1–
867 11. doi: 10.5194/os-13-1-2017
868
- 869 Bittig, H. C., Körtzinger, A., Neill, C., van Ooijen, E., Plant, J. N., Hahn, J., Johnson, K., S.,
870 Yang, B., & Emerson, S. R. (2018a), Oxygen optode sensors: principle, characterization,
871 calibration and application in the ocean. *Frontiers in Marine Science*, 4:429. doi:
872 [10.3389/fmars.2017.00429](https://doi.org/10.3389/fmars.2017.00429)
873
- 874 Bittig H.C., Steinhoff, T., Claustre, H., Fiedler, B., Williams, N. L., Sauzède, R., Körtzinger, A.,
875 & Gattuso, J.P. (2018b), An Alternative to Static Climatologies: Robust Estimation of Open
876 Ocean CO₂ Variables and Nutrient Concentrations From T, S, and O₂ Data Using Bayesian
877 Neural Networks. *Frontiers in Marine Science*. 5:328. doi: 10.3389/fmars.2018.00328
878
- 879 Bittig, H.C., Maurer, T.L., Plant, J.N., Schmechtig, C., Wong, A.P.S., Claustre, H., Trull, T.W.,
880 Udaya Bhaskar, T.V.S., Boss, E., Dall’Olmo, G., Organelli, E., Poteau, A., Johnson, K.S.,
881 Hanstein, C., Leymarie, E., Le Reste, S., Riser, S.C., Rupan, A.R., Taillandier, V., Thierry, V. &
882 Xing, X. (2019), A BGC-Argo Guide: Planning, Deployment, Data Handling and
883 Usage. *Frontiers in Marine Science*, 6:502. doi: 10.3389/fmars.2019.00502
884
- 885 Bronselaer, B., Winton, M., Griffies, S.M., Stouffer, R.J., Hurlin, W.J., Sergienko, O.V.,
886 Rodgers, K., & Russell, J. (2018), Change in future climate due to Antarctic
887 meltwater. *Nature*, 564, 53–58. <https://doi.org/10.1038/s41586-018-0712-z>
888

- 889 Bushinsky, S. M., Emerson, S. R., Riser, S. C., & Swift, D. D. (2016), Accurate oxygen
 890 measurements on modified Argo floats using in situ air calibrations. *Limnology and*
 891 *Oceanography Methods*, 14: 491-505. doi:10.1002/lom3.10107
 892
- 893 Bushinsky, S. M., Landschützer, P., Rödenbeck, C., Gray, A. R., Baker, D., Mazloff, M. R., et al.
 894 (2019a), Reassessing Southern Ocean air-sea CO₂ flux estimates with the addition of
 895 biogeochemical float observations. *Global Biogeochemical Cycles*. 33, 1370–
 896 1388. <https://doi.org/10.1029/2019GB006176>
 897
- 898 Bushinsky, S.M., Takeshita, Y., & Williams, N.L. (2019b), Observing Changes in Ocean
 899 Carbonate Chemistry: Our Autonomous Future. *Current Climate Change Reports*. 5, 207–220
 900 <https://doi.org/10.1007/s40641-019-00129-8>
 901
- 902 Carter, B.R., Feely, R.A., Williams, N.L., Dickson, A.G., Fong, M.B., & Takeshita, Y. (2018),
 903 Updated methods for global locally interpolated estimation of alkalinity, pH, and nitrate.
 904 *Limnology and Oceanography Methods*, 16: 119-131. doi:[10.1002/lom3.10232](https://doi.org/10.1002/lom3.10232)
 905
- 906 D’Asaro, E. A., & McNeil, C. (2013), Calibration and Stability of Oxygen Sensors on
 907 Autonomous Floats. *Journal of Atmospheric and Oceanic Technology*, 30, pp. 1896-1906
 908
- 909 Drucker, R., & Riser, S. C. (2016), In situ phase-domain calibration of oxygen Optodes on
 910 profiling floats. *Methods in Oceanography*, 17, 296-318,
 911 <https://doi.org/10.1016/j.mio.2016.09.007>.
 912
- 913 Fabozzi, F. J., Focardi, S. M., Rachev, S. T., & Arshanapalli, B. G. (2014), The Basics of
 914 Financial Econometrics: Tools, Concepts, and Asset Management Applications. Appendix E:
 915 Model Selection Criterion: AIC and BIC. Hoboken, New Jersey: Wiley & Sons, Inc.
 916
- 917 Ford, D. (2021), Assimilating synthetic Biogeochemical-Argo and ocean colour observations
 918 into a global ocean model to inform observing system design. *Biogeosciences*, 18, 509–534,
 919 <https://doi.org/10.5194/bg-18-509-2021>.
 920
- 921 Gaillard, F., Autret, E., Thierry, V., Galaup, P., Coatanoan, C., & Loubrieu, T. (2009), Quality
 922 control of large Argo datasets. *Journal of Atmospheric and Oceanic Technology*, 26, 337-351,
 923 doi:10.1175/2008JTECHO552.1.
 924
- 925 Garcia, H. E. & Gordon, L. I. (1992), Oxygen solubility in seawater: Better fitting
 926 equations. *Limnology and Oceanography*, 37, doi: 10.4319/lo.1992.37.6.1307.
 927
- 928 Gordon, C., Fennel, K., Richards, C., Shay, L. K., & Brewster, J. K. (2020), Can ocean
 929 community production and respiration be determined by measuring high-frequency oxygen
 930 profiles from autonomous floats? *Biogeosciences*, 17, 4119-4134, doi: 10.5194/bg-17-4119-2020
 931
- 932 Gray, A., Johnson, K. S., Bushinsky, S. M., Riser, S. C., Russell, J. L., Talley, L. D.,
 933 Wanninkhof, R., Williams, N. L., & Sarmiento, J. L. (2018), Autonomous biogeochemical floats

- 934 detect significant carbon dioxide outgassing in the high-latitude Southern Ocean. *Geophysical*
935 *Research Letters*, 45, 9049–9057. <https://doi.org/10.1029/2018GL078013>
- 936
- 937 Guinehut, S., Coatanoan, C., Dhomps, A. L., Le Traon, P. Y., & Larnicol, G. (2009), On the use
938 of satellite altimeter data in Argo quality control. *Journal of Atmospheric and Oceanic*
939 *Technology*, 26, 395-402. <https://doi.org/10.1175/2008JTECHO648.1>
- 940
- 941 Helm, K. P., Bindoff, N. L., & Church, J. A. (2011), Observed decreases in oxygen content of
942 the global ocean, *Geophysical Research Letters*, 38, L23602, doi:10.1029/2011GL049513.
- 943
- 944 Hood, E. M., Sabine, C. L., & Sloyan, B. M. eds. (2010), The GO-SHIP Repeat Hydrography
945 Manual: A Collection of Expert Reports and Guidelines. IOCCP Report Number 14, ICPO
946 Publication Series Number 134. Available online at <http://www.go-ship.org/HydroMan.html>.
- 947
- 948 Johnson, K. S., Coletti, L., Jannasch, H., Sakamoto, C., Swift, D. & Riser, S. (2013), Long-term
949 nitrate measurements in the ocean using the in situ ultraviolet spectrophotometer: Sensor
950 integration into the apex profiling float, *Journal of Atmospheric and Oceanic*
951 *Technology*, 30, 1854– 1866, doi:[10.1175/JTECH-D-12-00221.1](https://doi.org/10.1175/JTECH-D-12-00221.1).
- 952
- 953 Johnson, K. S., Plant, J. N., Riser, S. C., & Gilbert, D. (2015), Air oxygen calibration of oxygen
954 optodes on a profiling float array. *Journal of Atmospheric and Oceanic Technology*. 32, 2160-
955 2172.
- 956
- 957 Johnson, K. S., Jannasch, H. W., Coletti, L. J., Elrod, V. A., Martz, T. R., Takeshita, Y., Carlson,
958 R. J., & Connery J. J. (2016), Deep-Sea DuraFET: A pressure tolerant pH sensor designed for
959 global sensor networks, *Analytical Chemistry*. doi:[10.1021/acs.analchem.5b04653](https://doi.org/10.1021/acs.analchem.5b04653).
- 960
- 961 Johnson, K. S., Plant, J. N., Coletti, L. J., Jannasch, H. W., Sakamoto, C. M., Riser, S. C., Swift,
962 D. D., Williams, N. L., Boss, E., Haëntjens, N., Talley, L. D., & Sarmiento, J. L. (2017),
963 Biogeochemical sensor performance in the SOCCOm profiling float array. *Journal of*
964 *Geophysical Research Oceans*, 122, 6416–6436, doi:10.1002/2017JC012838.
- 965
- 966 Johnson, K. S., Pasqueron De Fommervault, O., Serra, R., D'Ortenzio, F., Schmechtig, C.,
967 Claustre, H., & Poteau, A. (2018a), Processing Bio-Argo nitrate concentration at the DAC Level.
968 Argo data management. <https://doi.org/10.13155/46121>
- 969
- 970 Johnson K. S., Plant J. N., & Maurer T. L., (2018b), Processing BGC-Argo pH data at the DAC
971 level. Argo data management. <https://doi.org/10.13155/57195>
- 972
- 973 Johnson, K. S., Riser, S. C., & Ravichandran, M. (2019), Oxygen variability controls
974 denitrification in the Bay of Bengal oxygen minimum zone. *Geophysical Research*
975 *Letters*, 46, 804– 811. <https://doi.org/10.1029/2018GL079881>
- 976
- 977 Kalnay, E. M., and Coauthors. (1996), The NCEP/NCAR 40-Year Reanalysis Project. *Bull.*
978 *American Meteorological Society*, 77, 437–470, doi:10.1175/1520-
979 0477(1996)077,0437:TNYRP.2.0.CO;2.

- 980
981 Kass, R. E., & Raferty, A. E. (1995), Bayes Factors. *Journal of the American Statistical*
982 *Association*, 90: 773-795.
- 983
984 Killick R., Fearnhead, P., & Eckley, I.A. (2012), Optimal detection of changepoints with a linear
985 computational cost. *Journal of the American Statistical Association*, 107: 1590-1598.
- 986
987 Mignot, A., D'Ortenzio, F., Taillandier, V., Cossarini, G., & Salon, S. (2019), Quantifying
988 observational errors in Biogeochemical-Argo oxygen, nitrate, and chlorophyll *a* concentrations.
989 *Geophysical Research Letters*, 46, 4330– 4337. <https://doi.org/10.1029/2018GL080541>
- 990
991 Nicholson, D. P., & Feen, M. L. (2017), Air calibration of an oxygen optode on an underwater
992 glider. *Limnology and Oceanography Methods*, 15: 495-502. doi:10.1002/lom3.10177
- 993
994 Olsen, A., Lange, N., Key, R. M., Tanhua, T., Bittig, H. C., Kozyr, A., Álvarez, M., Azetsu-
995 Scott, K., Becker, S., Brown, P. J., Carter, B. R., Cotrim da Cunha, L., Feely, R. A., van
996 Heuven, S., Hoppema, M., Ishii, M., Jeansson, E., Jutterström, S., Landa, C. S., Lauvset, S. K.,
997 Michaelis, P., Murata, A., Pérez, F. F., Pfeil, B., Schirnack, C., Steinfeldt, R., Suzuki, T.,
998 Tilbrook, B., Velo, A., Wanninkhof, R., & Woosley, R. J. (2020), GLODAPv2.2020 – the
999 second update of GLODAPv2. doi:10.5194/essd-2020-165.
- 1000
1001 Owens, B. W., & Wong, A. P. S. (2009). An improved calibration method for the drift of the
1002 conductivity sensor on autonomous CTD profiling floats by θ -S climatology. *Deep-Sea*
1003 *Research Part I – Ocean Research Papers*, 56, 450-457. doi:10.1016/j.dsr.2008.09.008.
- 1004
1005 Ríos, A. F., Resplandy, L., García-Ibáñez, M. I., Fajar, N. M., Velo, A., Padin, X. A., et al.
1006 (2015), Decadal acidification in the water masses of the Atlantic Ocean. *Proceedings of the*
1007 *National Academy of Sciences*, 112(32), 9950–9955. <https://doi.org/10.1073/pnas.1504613112>
- 1008
1009 Riser, S. C., Swift, D., & Drucker, R. (2018), Profiling floats in SOCCOM: Technical
1010 capabilities for studying the Southern Ocean. *Journal of Geophysical Research: Oceans*, 123,
1011 4055–4073. <https://doi.org/10.1002/2017JC013419>
- 1012
1013 Roemmich, D., Alford, M. H., Claustre, H., Johnson, K., King, B., Moum, J., Oke, P.,
1014 Owens, W. B., Pouliquen, S., Purkey, S., Scanderbeg, M., Suga, T., Wijffels, S., Zilberman, N.,
1015 Bakker, D., Baringer, M., Belbeoch, M., Bittig, H. C., Boss, E., Calil, P., Carse, F., Carval, T.,
1016 Chai, F., Conchubhair, D. O., d'Ortenzio, F., Dall'Olmo, G., Desbruyeres, D., Fennel, K., Fer, I.,
1017 Ferrari, R., Forget, G., Freeland, H., Fujiki, T., Gehlen, M., Greenan, B., Hallberg, R.,
1018 Hibiya, T., Hosoda, S., Jayne, S., Jochum, M., Johnson, G. C., Kang, K., Kolodziejczyk, N.,
1019 Körtzinger, A., Le Traon, P.-Y., Lenn, Y.-D., Maze, G., Mork, K. A., Morris, T., Nagai, T.,
1020 Nash, J., Garabato, A. N., Olsen, A., Pattabhi, R. R., Prakash, S., Riser, S., Schmechtig, C.,
1021 Schmid, C., Shroyer, E., Sterl, A., Sutton, P., Talley, L., Tanhua, T., Thierry, V., Thomalla, S.,
1022 Toole, J., Troisi, A., Trull, T. W., Turton, J., Velez-Belchi, P. J., Walczowski, W., Wang, H.,
1023 Wanninkhof, R., Waterhouse, A. F., Waterman, S., Watson, A., Wilson, C., Wong, A. P. S.,
1024 Xu, J., & Yasuda, I. (2019). On the Future of Argo: A Global, Full-Depth, Multi-Disciplinary
1025 Array, *Frontiers in Marine Science*, 6, 439, <https://doi.org/10.3389/fmars.2019.00439>

- 1026
1027 Russell, J. L., Kamenkovich, I., Bitz, C., Ferrari, R., Gille, S. T., Goodman, P. J., Hallberg, R.,
1028 Johnson, K., Khazmutdinova, K., Marinov, I., Mazloff, M., Riser, S., Sarmiento, J. L., Speer, K.,
1029 Talley, L. D. & Wannikhof, R. (2018), Metrics for the Evaluation of the Southern Ocean in
1030 Coupled Climate Models and Earth System Models. *Journal of Geophysical Research: Oceans*,
1031 123, 3120-3143. <https://doi.org/10.1002/2017JC013461>
1032
- 1033 Salstein, D. A., Ponte, R. M., & Cady-Pereira, K. (2018), Uncertainties in atmospheric surface
1034 pressure fields from global analyses, *J. Geophys. Res.*, 113, D14107,
1035 doi:10.1029/2007JD009531, 2008.
1036
- 1037 Sampson, D. (2021), GUI Layout Toolbox
1038 (<https://www.mathworks.com/matlabcentral/fileexchange/47982-gui-layout-toolbox>), MATLAB
1039 Central File Exchange.
1040
- 1041 Sauzède R., Bittig, H.C., Claustre, H., Pasqueron de Fommervault, O., Gattuso, J-P, Legendre,
1042 L., & Johnson, K.S. (2017), Estimates of Water-Column Nutrient Concentrations and Carbonate
1043 System Parameters in the Global Ocean: A Novel Approach Based on Neural
1044 Networks. *Frontiers in Marine Science*, 4:128. doi: 10.3389/fmars.2017.00128
1045
- 1046 Schmechtig, C., Thierry, V., & The Bio Argo Team. (2016), Argo quality control manual for
1047 biogeochemical data. <https://doi.org/10.13155/40879>
1048
- 1049 Swart, S., Gille, S. T., Delille, B., Josey, S., Mazloff, M., Newman, L., Thompson, A.F.,
1050 Thomson, J., Ward, B., du Plessis, M.D., Kent, E.C., Girton, J., Gregor, L., Heil, P., Hyder, P.,
1051 Pezzi, L.P., de Souza, R.B., Tamsitt, V., Weller, R.A., & Zappa, C.J. (2019), Constraining
1052 Southern Ocean Air-Sea-Ice Fluxes Through Enhanced Observations. *Frontiers in Marine
1053 Science*, 6:421. doi: 10.3389/fmars.2019.00421
1054
- 1055 Takeshita, Y., Martz, T. R., Johnson, K. S., Plant, J. N., Gilbert, D., Riser, S. C., Neill, C., &
1056 Tilbrook, B. (2013), A climatology-based quality control procedure for profiling float oxygen
1057 data. *Journal of Geophysical Research Oceans*, 118, 5640-5650. doi:10.1002/jgrc.20399
1058
- 1059 Takeshita, Y., Jones, B. D., Johnson, K. S., Chavez, F. P., Rudnick, D. L., Blum, M., Conner, K.,
1060 Jensen, S., Long, J. S., Maughan, T., Mertz, K. L., Sherman, J. T., & Warren, J. (2020), Accurate
1061 pH and O₂ measurements from Spray underwater gliders. *Journal of Atmospheric and Oceanic
1062 Technology*, <https://doi.org/10.1175/JTECH-D-20-0095.1>
1063
- 1064 Thierry, V, Bittig, H., Gilbert, D., Kobayashi, T., Kanako, S., & Schmid, C. (2018), Processing
1065 Argo oxygen data at the DAC level. <https://doi.org/10.13155/39795>
1066
- 1067 Thierry V., Bittig., The Argo-BGC Team (2018b), Argo quality control manual for dissolved
1068 oxygen concentration. <https://doi.org/10.13155/46542>
1069

- 1070 Verdy, A., & Mazloff, M. R. (2017), A data assimilating model for estimating Southern Ocean
1071 biogeochemistry. *Journal of Geophysical Research Oceans*, 122, 6968–6988,
1072 doi:10.1002/2016JC012650.
- 1073
1074 Williams, N. L., Juranek, L. W., Johnson, K. S., Feely, R. A., Riser, S. C., Talley, L. D., Russell,
1075 J. L., Sarmiento, J. L. & Wanninkhof, R. (2016), Empirical algorithms to estimate water column
1076 pH in the Southern Ocean. *Geophys. Res. Lett.*, 43, 3415–3422, doi:10.1002/2016GL068539.
- 1077
1078 Williams, N. L., Juranek, L. W., Feely, R. A., Russell, J. L., Johnson, K. S., & Hales,
1079 B. (2018), Assessment of the carbonate chemistry seasonal cycles in the Southern Ocean from
1080 persistent observational platforms. *Journal of Geophysical Research: Oceans*, 123, 4833–
1081 4852. <https://doi.org/10.1029/2017JC012917>
- 1082
1083 Wong, A. P. S., Johnson, G. C., & Owens, W. B. (2003), Delayed-mode calibration of
1084 autonomous CTD profiling float salinity data by θ -S climatology. *Journal of Atmospheric and*
1085 *Oceanic Technology*, 20, 308-318. [https://doi.org/10.1175/1520-0426\(2003\)020,0308:](https://doi.org/10.1175/1520-0426(2003)020,0308:DMCOAC.2.0.CO;2)
1086 [DMCOAC.2.0.CO;2](https://doi.org/10.1175/1520-0426(2003)020,0308:DMCOAC.2.0.CO;2).
- 1087
1088 Wong, A. P. S. & Riser, S. C. (2011), Profiling Float Observations of the Upper Ocean under
1089 Sea Ice off the Wilkes Land Coast of Antarctica. *Journal of Physical Oceanography*, 41(6),
1090 1102– 1115.
- 1091
1092 Wong, A.P.S., S.E. Wijffels, S.C. Riser, S. Pouliquen, S. Hosoda, D. Roemmich, J. Gilson,
1093 G.C. Johnson, K. Martini, D.J. Murphy, M. Scanderbeg, T.V.S.U. Bhaskar, J.J.H. Buck, F.
1094 Merceur, T. Carval, G. Maze, C. Cabanes, X. André, N. Poffa, I. Yashayaev, P.M. Barker, S.
1095 Guinehut, M. Belbéoch, M. Ignaszewski, M.O.N. Baringer, C. Schmid, J.M. Lyman, K.E.
1096 McTaggart, S.G. Purkey, N. Zilberman, M.B. Alkire, D. Swift, W.B. Owens, S.R. Jayne, C.
1097 Hersh, P. Robbins, D. West-Mack, F. Bahr, S. Yoshida, P.J.H. Sutton, R. Cancouët, C.
1098 Coatanoan, D. Dobbler, A. Garcia Juan, J. Gourrion, N. Kolodziejczyk, V. Bernard, B. Bourlès,
1099 H. Claustre, F. D’Ortenzio, S. Le Reste, P.-Y. Le Traon, J.-P. Rannou, C. Saout-Grit, S. Speich,
1100 V. Thierry, N. Verbrugge, I.M. Angel-Benavides, B. Klein, G. Notarstefano, P.-M. Poulain, P.
1101 Vélez-Belchí, T. Suga, K. Ando, N. Iwasaska, T. Kobayashi, S. Masuda, E. Oka, K. Sato, T.
1102 Nakamura, K. Sato, Y. Takatsuki, T. Yoshida, R. Cowley, J.L. Lovell, P.R. Oke, E.M. van Wijk,
1103 F. Carse, M. Donnelly, W.J. Gould, K. Gowers, B.A. King, S.G. Loch, M. Mowat, J. Turton,
1104 E.P. Rama Rao, M. Ravichandran, H.J. Freeland, I. Gaboury, D. Gilbert, B.J.W. Greenan, M.
1105 Ouellet, T. Ross, A. Tran, M. Dong, Z. Liu, J. Xu, K. Kang, H. Jo, S.-D. Kim & H.-M. Park
1106 (2020), Argo Data 1999–2019: Two Million Temperature-Salinity Profiles and Subsurface
1107 Velocity Observations from a Global Array of Profiling Floats, *Frontiers in Marine*
1108 *Science*, 7, <https://doi.org/10.3389/fmars.2020.00700>